Assessing the Sources of the O^+ in the Plasma Sheet

J. Liao[1], L. M. Kistler[1], C. G. Mouikis[1], S. A. Fuselier[23], M. Hedlund[1]

1 Department of Physics and Space Science Center, University of New Hampshire, Durham, New Hampshire, USA

2 Southwest Research Institute

3 University of Texas at San Antonio

Corresponding author: Jing Liao (jing.liao@unh.edu)

† Department of Physics and Space Science Center, University of New Hampshire, Durham, NH 03824, USA.

Key Points:

- Cusp-source O^+ is observed entering the plasma sheet from the lobe throughout the <25 R_E magnetotail.
- The nightside auroral-source O^+ is identified at <100 eV inside 10 R_E, with a more energetic component further out on the duskside.
- We estimate that during quiet times, the nightside auroral contribution to the near-earth plasma sheet O^+ exceeds the cusp contribution.

Abstract

To study the contributions of cusp outflow coming through the lobes and nightside auroral outflow to the O^+ in the plasma sheet, we performed a statistical study of tailward streaming O^+ in the lobes, the plasma sheet boundary layer (PSBL) and the plasma sheet (PS), using MMS/HPCA data. Similar spatial distributions demonstrate the entry of cusp-origin O^+ from the lobes to the plasma sheet through the PSBL. There is an energy dependence in the lobe O^+ spatial distribution, with low-energy O^+ streaming near the center in Y_{GSM} while high energy (1-3 keV) O^+ streams near the flanks. Low energy (< 100 eV) O^+ from the nightside auroral oval can be identified in the near-Earth PSBL/PS with high-density (> 0.03 cm^{-3}), and energetic (> 3 keV) streaming O^+ with similar density (~0.02 cm^{-3}) is seen further out on the duskside of the PSBL/PS. The rest of the nightside auroral O^+ in the PSBL is mixed with O^+ coming in from the lobe, and difficult to distinguish. We estimated the inflow and outflow of ions in the plasma sheet between 7-17 R_E, using data extracted from previous studies and this work. Comparisons between the estimated fluence suggest that the majority of near-Earth plasma sheet H^+ are from cusps and Earthward convection from the distant tail. The O^+ in the same region, on the other hand, has a mixed source, with auroral outflow giving the highest contribution.

Plain Language Summary

We studied the sources of the plasma sheet, using MMS/HPCA data. We observed and mapped the location of the Oxygen ions streaming from the dayside cusp region entering the plasma sheet through the plasma sheet boundary layer. The observations of the Oxygen ions from the nightside auroral oval streaming inside the plasma sheet boundary layer show that this population has higher density than the dayside cusp origin Oxygen ions. We estimated the number of the proton and Oxygen ions ions per second entering and leaving the plasma sheet and conclude that the solar wind proton is the major source for plasma sheet proton and ionospheric Oxygen ions from the nightside auroral oval is the major source for Oxygen ions in the plasma sheet.

1 Introduction

The Earth's magnetosphere contains ion populations from both the solar wind and ionosphere. Heavy O^+ ions, originating from the ionosphere, can dominate the ring current energy density during geomagnetic storm times. Energetic O^+ ions in the plasma sheet (PS) directly impact the storm time ring current O^+ content. Previous studies (Kistler et al., 2016; Keika et al., 2013) show that adiabatic inward transport of the hot plasma sheet population at ~6 R_E contributes to the dominant pressure that drives the storm time ring current. Thus, understanding this near-Earth hot plasma sheet population is one of the keys to predicting the strength of the ring current.

Comparisons between the plasma sheet composition at 15-20 R_E (Mouikis et al., 2010) and around 6 R_E (Kistler and Mouikis et al., 2016) show that the O^+/H^+ ratio increases with decreasing radial distance. One explanation is that there may be significant entry of O^+ to the plasma sheet near the Earth. There are two sources for the direct entry of O^+ to the plasma sheet: the cusp and the nightside aurora. The significant entry near the Earth could be from either or both sources.

Ions outflowing from the dayside cusp region move across the polar caps and travel along the open field lines in the lobes, with the convection from the dawn-dusk magnetospheric electric field moving them toward the central current sheet. While some ions are lost in the distant tail, others may enter the plasma sheet during tail reconnection and convect Earthward. Moore et al. (2005) showed the difference between entry of ions near the Earth and further down the tail. Ions with lower energy (< 1 keV) may reach the plasma sheet close to the Earth, where the field is close to dipolar. Those ions will remain close to field-aligned and mirror while drifting eastward with little energy gain, contributing to the warm plasma cloak. If the ions are more energetic (> 1 keV), they may reach the plasma sheet further down the tail where the plasma sheet is stretched. Those ions will then be scattered, heated, becoming part of the hot isotropic plasma sheet. The behavior depends on the particle gyroradius, compared to the curvature of the neutral sheet. At 15-19 R_E, the Cluster spacecraft observed the cusp origin ions entering the plasma sheet far enough down the tail to become isotropic and heated, becoming part of the hot plasma sheet (e.g., Kistler et al., 2010). During storm times, the intensity of cusp source ions increases, and the entry into the plasma sheet may last for many hours. Ionospheric ions from the nightside aurora region travel along the closed field lines and may enter the plasma sheet through the plasma sheet boundary layer (PSBL). The outflow is usually bursty. The intensity varies both with substorms and storms. Lower energy ions enter the plasma sheet near the Earth, and remain at low energy, while higher energy ions enter further down the tail, and may become isotropic, heated, and become part of the hot plasma sheet.

Adapted from (Kistler et al., 2019), Figure 1 shows the trajectories of particles with different initial energies from the two different outflow regions. For both regions, when the ions of different energies flow out from the source, they are convected towards the center at the same speed. As a result, the trajectories of ions are separated due to their initial energies, with energetic ions reaching further down the tail and low-energy ions trapped near the Earth. Dayside cusp origin ions move along the open field lines, become dispersed, and gain energy from centrifugal acceleration as they move out. Nightside aurora origin ions following closed field lines are also dispersed by energy as they enter the plasma sheet. As a result, in the in-situ observations, spatial difference will lead to an energy difference.

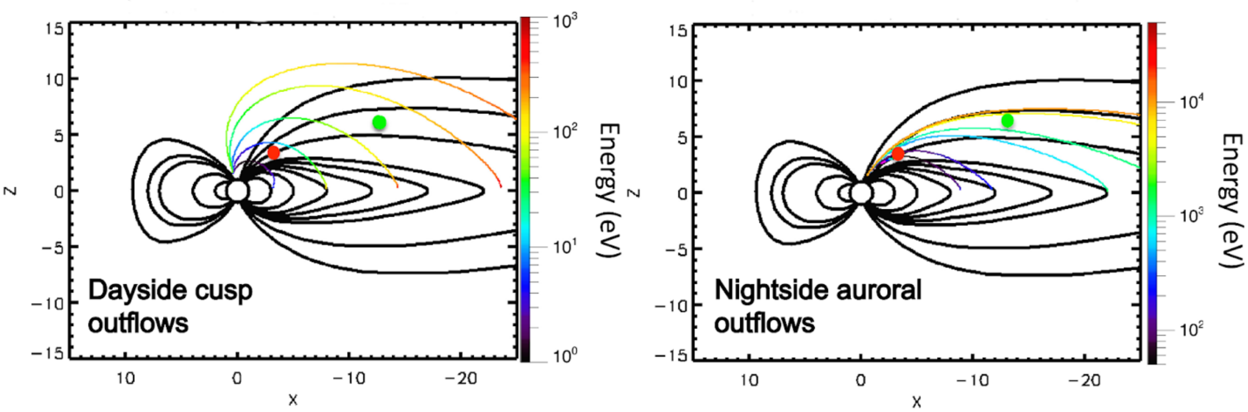

Figure 1. Simulated velocity filter effect for ions from dayside cusp and nightside aurora. Adapted from [Kistler et al. 2019]

Ionospheric outflow from both the dayside cusp and nightside auroral region increase during geomagnetic active time (Moore et al., 1999; Nosè et al., 2003, Kistler et al. 2006). The transport path of the O^+ is also strongly affected by geomagnetic activity (Liao et al. 2010). Enhanced convection during geomagnetic storms can lead to stronger centrifugal acceleration for the cusp outflowing O^+ and leading to more energetic O^+ inside the lobes (Cladis, 1986; Huddleston et al., 2005). Substorm-associated reconnections in the tail can bring more O^+ into the plasma sheet and lead to stronger Earthward convection than quiet times.

The enhancement of ionospheric outflow has been found to be strongly correlated with the solar wind drivers, in particular pressure and velocity (Cully et al., 2003; Elliott et al., 2001) through precipitation and the convection field. The solar wind pressure and velocity also affect the O^+ transport path inside the lobes through convection field (Liao et al., 2011). Increased EUV leads to stronger ionospheric outflow on both dayside and nightside (Strangeway et al., 2005; Zhao et al., 2020; Zhao et al., 2022).

The tailward moving, field-aligned O^+ observed in the lobes is mostly from the dayside cusp. Liao et al. 2010 studied the transport path of ionospheric O^+ from the dayside cusp with Cluster lobe observations. The study showed that O^+ ions from the dayside cusps are commonly observed in the lobes even during non-storm times. The occurrence rate of O^+ is even higher during storm time. There is an IMF By-driven asymmetry on the transport path of cusp origin O^+, which is strongest when IMF By is positive.

Tailward moving, field-aligned O^+ in the PSBL and plasma sheet could come from either source. In this paper, we present our statistical study of the O^+ entry into the PSBL and the plasma sheet: the spatial distribution of the observed ions, the energy and density distribution, and how their distribution varies depending on the driver. We will also discuss the average (mainly non-storm time) supply and loss of ions in the near-Earth plasma sheet.

2 Data

2.1 Spacecraft

The Cluster satellite has provided good measurements of O^+ in the lobe, but due to the polar orbit, there are fewer equatorial plasma sheet measurements from -6 to -15 R_E. Complementary to Cluster's lobe observations, Magnetospheric Multiscale (MMS) spacecraft spent extended time orbiting near the central plasma sheet region, which allows us to perform a statistical study of O^+ entry into the plasma sheet through the PSBL and the nightside entry of the O^+ from the nightside auroral source.

The MMS Mission was launched on March 13th, 2015, to study the Earth's magnetosphere, using four identical spacecraft flying in a tetrahedral formation. We use the MMS data from 2017 to 2020 which covers orbital distances out to 28 R_E. Figure 2 shows the orbital segments from 2017 to 2020 in XZ_{GSM}, and XY_{GSM} planes. The focus of the orbits is within the equatorial plane: orbits are confined within +/- 10 R_E in Z_{GSM}, providing great PSBL and plasma sheet coverage. The full coverage is not symmetrical between the north and south hemispheres, but orbit coverage between +/- 5 R_E is symmetrical enough for spatial distribution analysis. The orbits cover both positive and negative Y_{GSM} regions (dawn and dusk sides of the magnetosphere). We will not use the data collected on the dayside (MLT between 8 to 16) and outside $|Y_{GSM}| = 20\ R_E$

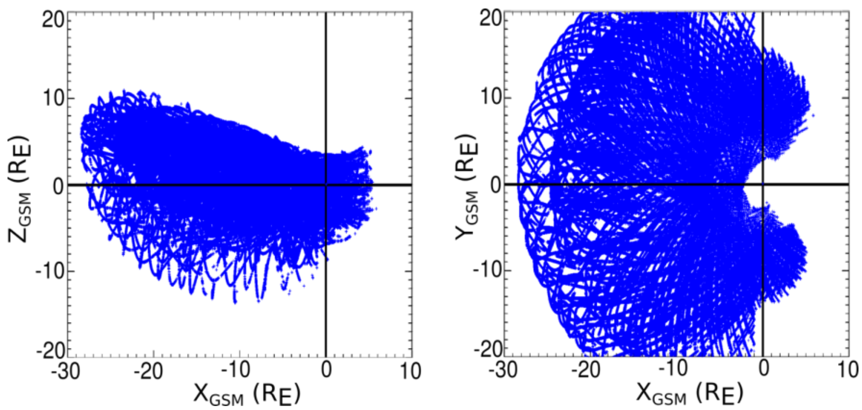

Figure 2. 2017-2020 orbital segments of MMS within the magnetosphere, in XZ_{GSM}, XY_{GSM} projection. Dayside observation is taken out.

Because MMS spacecraft are close to each other, and we average data over 5 minutes for better statistics, the data used in this study are essentially the same on different spacecraft for our purpose. Thus, we only used data collected by MMS1 in this study.

2.2 Instrument

Onboard each MMS spacecraft, the Hot Plasma Composition Analyzer (HPCA) (Young et al. 2016) is an instrument combining an electrostatic energy analyzer with a carbon-foil based time-of-flight analyzer. It measures the flux of H^+, He^{++}, He^+, and O^+ from 1 eV to 40 keV at 16 elevation anodes, with a time resolution of 10-15 seconds (Young et al., 2014). This study predominantly uses HPCA fast survey data, which sums the distribution into 8 elevation and 8 azimuthal angular bins, and 16 energy bins. The magnetic field used in this study is collected by Fluxgate Magnetometers (FGM) (Torbert et al. 2016). IDL Software based on the SPEDAS/TDAS package is used to extract data.

2.2.1 Compression Scheme Modes

For onboard memory usage optimization, HPCA data are collected under survey and burst modes (Young et al., 2016). The survey data stream is collected nearly continuously. All data collected in survey mode are downlinked to the ground after summation over energy-angle-

angle-TOF bins. The burst mode data stream is collected concurrently with the collection of survey mode data but at much higher resolution. The burst Data is downlinked to the ground without summation.

For some time periods used in this study, HPCA data was compressed with a lossy scheme before being downlinked to the ground. The lossy scheme drops all single-count data in any accumulated energy-angle-angle bin for each species. Under Survey mode, all single-count data are dropped after summation; under Burst mode, since there is no summation, all single-count data are dropped. The direct impact of the lossy scheme is that data may have significantly lower reported flux, especially for minor species and low energy populations, as minor species and lower energy bins with narrower energy bin ranges are more likely to have fewer counts. The impact is greater for isotropic populations than for anisotropic populations for the same total number of counts, and it affects Burst mode data more than Survey mode data.

The lossy scheme was in use most of the time before 2022-05-24. The compression was temporarily off under Fast Survey mode (Young et al., 2016) from 2018-05-27 to 2018-09-25 and for the entire orbit from 2019-04-16 to 2019-08-17. The lossy scheme was turned off after 2022-05-24.

As our study focuses on field-aligned O^+, which can be a relatively minor species, with low flux particularly at low energies, the lossy scheme had a significant impact on the data. In particular, it resulted in significant loss of O^+ in the lower energy range. To aggregate all the data from 2017 to 2020, including both compressed and non-compressed times, we analyzed the impact of the compression scheme on the occurrence frequency, median and minimum energy, and median density. We simulated the compression algorithm and applied it to the data collected during the time when compression scheme was off in 2018-2019.

For occurrence frequency, we compared the occurrence frequency maps with and without the compression and calculated empirical occurrence frequency correction factors to restore the occurrence frequency to the original level. All occurrence frequency results shown in this study are after the correction.

For energy results, we studied the compression scheme's impact on the median and minimum energy maps in all regions. The median value of the energy is higher when the data is compressed. The increase is smallest for lobes and higher for PSBL and the highest in the plasma sheet. However, the general patterns remain for the median energy maps for all regions. The conclusions are the same for the minimum energy maps. While we can use a region-related factor to correct the occurrence frequency, the impact of the compression scheme on the energy profile is more non-linear and difficult to compensate for. In the following sections, we present the median and minimum energy maps with the compressed data and uncompressed data after compression simulation to have a consistent dataset. The maps show the energy slightly higher than the actual value in median and minimum energy maps, but the general pattern of the maps remains the same.

The median density maps are the median value of densities of all the observed streaming O^+ in each bin. The compression scheme has minimal effect on the median density maps because the streaming O^+ is strongly anisotropic, concentrated in relatively few angular bins. Details of the compression scheme impact can be found in Appendix A.

3 Streaming O^+

3.1 Observations of streaming O^+

To study the transport path and entry of the ionospheric ions, we must first identify the O^+ from the dayside cusp or nightside aurora region traveling in different regions within the magnetosphere. Our goal is to identify the populations before they have become scattered and isotropized in the plasma sheet, which makes their source much more difficult to identify. To achieve this, we study the continuous outward/tailward moving, field-aligned populations, which we call “streaming O^+”. Due to the velocity filter effect, ions from both ionospheric sources will separate according to their velocity. As a result, we often observe streaming O^+ as a mono-energetic population with a strong flux in the energy spectra. Figure 3,4 and 5 present examples of observed streaming O^+ populations.

Figure 3 shows an example of a typical streaming O^+ event observed by MMS in the lobes, the PSBL, and the plasma sheet on July 1st, 2017. This is an example of the cusp-source ions coming in from the lobes to the PSBL and then into the plasma sheet, as has been shown in Kistler et al. (2010). The panels (a)-(d) are plasma β, H^+ energy spectra, O^+ energy spectra, O^+ pitch angle spectra. To study the parallel and antiparallel moving population separately, we calculate the flux per energy for O^+ with pitch angle between 0 and 60 degrees (parallel) and between 120 and 180 degrees (antiparallel). To remove isotropic and mirroring populations, we subtract antiparallel O^+ energy spectra from the parallel ones, and vice versa. Any negative values will be considered as zero. The results are shown in Figure 3e and Figure 3f. The black dots in the last panel show the identified streaming O^+. Bars between the panels indicate the

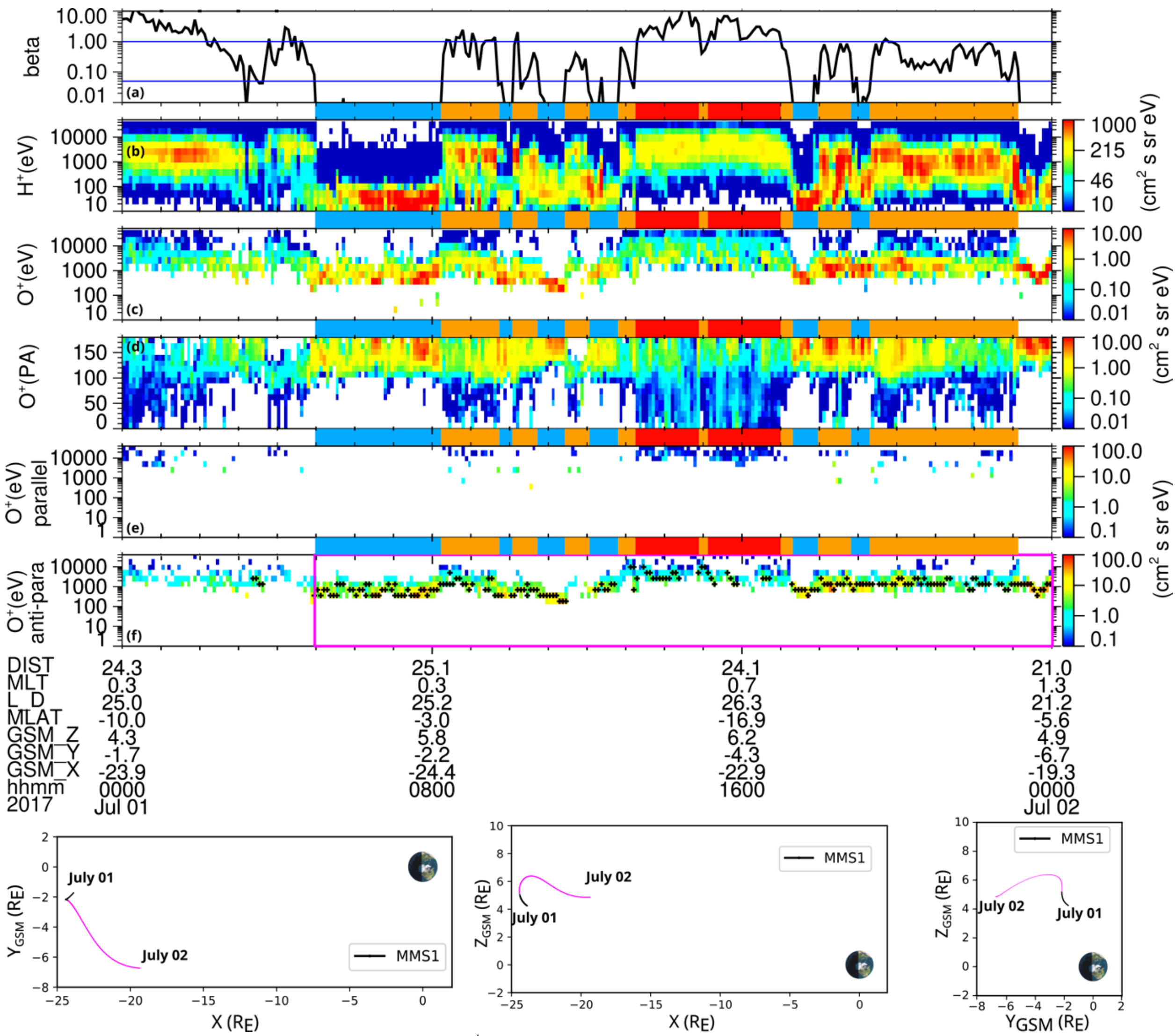

Figure 3. Observations of streaming O^+ from the dayside cusp. Panels from ton to down: Panel (a) is plasma beta. Panel (b) is proton energy spectra over all angles. Panel (c) is O^+ energy spectra over all angles. Panel (d) is the pitch angle of O^+ at all energy. Panel (e) is the energy spectra of parallel O^+ with pitch angle between 0 and 60 degrees. Panel (f) is the energy spectra of antiparallel O^+ with pitch angle between 120 and 180 degrees. Black dots in panel (f) show the identified streaming O^+. Bars between the energy spectra indicate the regions of the satellite: blue means lobe, orange means BL, and red means the plasma sheet. MMS orbits are shown in projections of XY_{GSM}, XZ_{GSM} and YZ_{GSM} at the bottom of the figure.

regions of the satellite: blue means lobe, orange means PSBL, and red means the plasmasheet. Plasma β is defined as the sum of proton and oxygen pressure divided by magnetic pressure. We use the plasma β to divide the region into lobe ($\beta < 0.05$), PSBL ($\beta > 0.05$ and $\beta < \beta 1$), and the plasma sheet ($\beta > \beta 1$) (Miyashita et al., 2020). $\beta 1$ is defined as

$$\beta 1 = 1 \qquad \text{at } R \geq 15\ R_E$$

$$\text{Log}_{10}(\beta 1) = 0.14R - 2.1 \qquad \text{at } R < 15\ R_E$$

Where $R = \sqrt{X^2 + Y^2}$

In Figure 3, from 05:00 to 08:00, a streaming O^+ population at around 1 KeV is observed in lobes shown as the yellow/red band in the O^+ energy spectra (panel c). In the O^+ pitch angle spectra (panel d), we can see this high flux population is mostly field aligned in the antiparallel direction. During observation time, MMS is in the northern hemisphere, so the observed anti-parallel streaming heavy ions are outflowing from the source. A similar streaming population is observed in the H^+ spectra with a lower energy (< 100 eV) that is roughly 16 times lower than the streaming O^+, implying that ions of different species are grouped/separated by their velocities. Afte 08:00, the spacecraft moves in and out between the lobes and the PSBL due to the dynamic movement of the magnetosphere, and the streaming O^+ is observed during the whole time. Eventually at ~13:20, the MMS enters the plasma sheet. The intense flux of the streaming population makes it stand out from the background population in the lobes and the PSBL. The flux becomes less intense when the ions enter the plasma sheet, get scattered and become isotropic, and the energy increases, implying possible acceleration during the entry. Similar characteristics have been observed and discussed in Kistler et al. 2010. MMS/HPCA observes the streaming O^+ population during the whole plasma sheet encounter and continues to witness it as the satellite leaves the plasma sheet and goes back into the lobe/PSBL regions. No streaming O^+ is observed in the parallel direction, confirming that the heavy ions are the outflowing population. During the observation time, the magnetosphere is quiet, with KP index peaking at 3 and the lowest Dst index is -13 nT.

Figure 4 shows an example of observation of energetic streaming O^+ observed in the lobe region near the magnetosheath. The panels are in the same arrangement as in figure 3. At the start of the 2019-10-25, the satellite was in the sheath, with high plasma beta, strong proton flux over a wide range. The population observed in O^+ is background contamination from the high H^+ rate during this time. At around 05:00, MMS enters the lobe and remains until 16:00, except for brief excursions to the PSBL. As marked by the black marks in figure 4e, streaming O^+ is observed during most of the time that MMS is in the lobe. At the bottom of figure 4 are the orbits

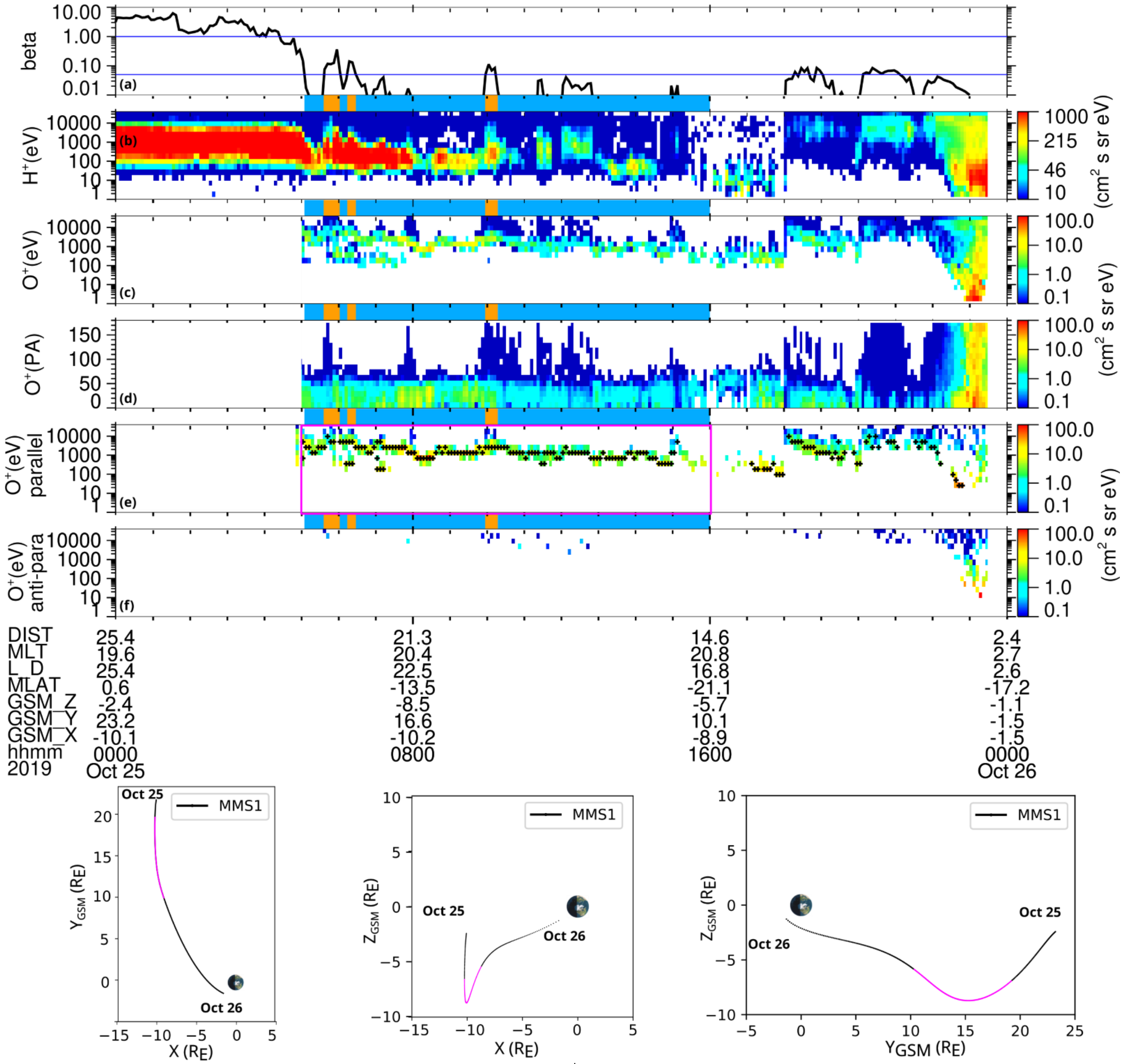

Figure 4. Observations of energetic streaming O^+ near the flanks. Panels from ton to down: Panel (a) is plasma beta. Panel (b) is proton energy spectra over all angles. Panel (c) is O^+ energy spectra over all angles. Panel (d) is the pitch angle of O^+ at all energy. Panel (e) is the energy spectra of parallel O^+ with pitch angle between 0 and 60 degrees. Panel (f) is the energy spectra of antiparallel O^+ with pitch angle between 120 and 180 degrees. Black dots in panel (e) show the identified streaming O^+. Bars between the energy spectra indicate the regions of the satellite: blue means lobe and orange means BL. MMS orbits are shown in projections of XY_{GSM}, XZ_{GSM} and YZ_{GSM} at the bottom of the figure.

of the MMS during the observation time, with the pink part of the orbit matches the pink box in panel (e). The YZ_{GSM} orbit shows that during the observation time of the lobe streaming O^+, the Z_{GSM} ranges from -5 R_E to -9 R_E, which is a typical southern lobe region, and Y_{GSM} ranges from 10 R_E to 20 R_E, which is on the dusk flank near the sheath. X_{GSM} is near -10 R_E the whole time. The streaming O^+ is very energetic (> 300 eV) during the observation, and the energy is higher when YGSM is larger. The highest observed streaming population is at 5 KeV when Y_{GSM} is around -19 R_E. The energetic lobe streaming O^+ and the correlation between Y_{GSM} and the energy of cusp source O^+ streaming will be discussed again in section 4.4.

Figure 5 shows an example of observation of nightside auroral outflows on 2020-10-27. The left panels are in the same arrangement as in figure 3 and 4 but without plasma beta. The three panels on the right show the orbit of the MMS during the observation in XY_{GSM}, XZ_{GSM} and YZ_{GSM} projections. The pink segment of the orbit corresponds to the observation time of the pink box in panel (d). MMS moves from X = -8 R_E towards the Earth, till X is less than -2 R_E, and from the southern hemisphere at around Z= -7 R_E towards the equatorial plane near Z= -1 R_E. During the whole observation time, MMS is on the nightside of the Earth. Starting from 07:50, MMS detects clear outflowing (parallel streaming in southern hemisphere) O^+, and then continuously observes streaming O^+ until 10:10, as shown in figure 5d. The energy of the observed streaming O^+ is high (> 1 keV) at the start, and gradually decreases. At the end of the observation of the streaming O^+, around 10:10, the O^+ is as low as ~10 eV, and the satellite is less than 5 R_E from the Earth. Another dispersion of higher energy in parallel direction is observed at the start of the pink box (09:45). Dispersions are also seen in the anti-parallel direction of different energies. The multiple dispersive streaming O^+ have been observed previously (Sauvaud et al., 2004; Gkioulidou et al., 2019; Liu, Z.-Y., & Zong, Q.-G., 2022). They are likely to be the direct injection from the northern and southern auroral ovals, and the O^+ bounced back from the mirroring points. The dispersive pattern is both temporal and spatial. Ions from the same sources are separated by their velocity as the faster ions arrive at the location first and the slower ones later. The velocity filter effect separates the ions by their velocities. Slow ions are convected inward more during their time moving up the field line, and so end up closer to the Earth. The lowest energy outflowing O^+, as shown in the pink box and the pink segment in the orbit, is observed near the Earth. Later our statistical study will show the low energy streaming O^+ in the PS and PSBL are only observed near the Earth.

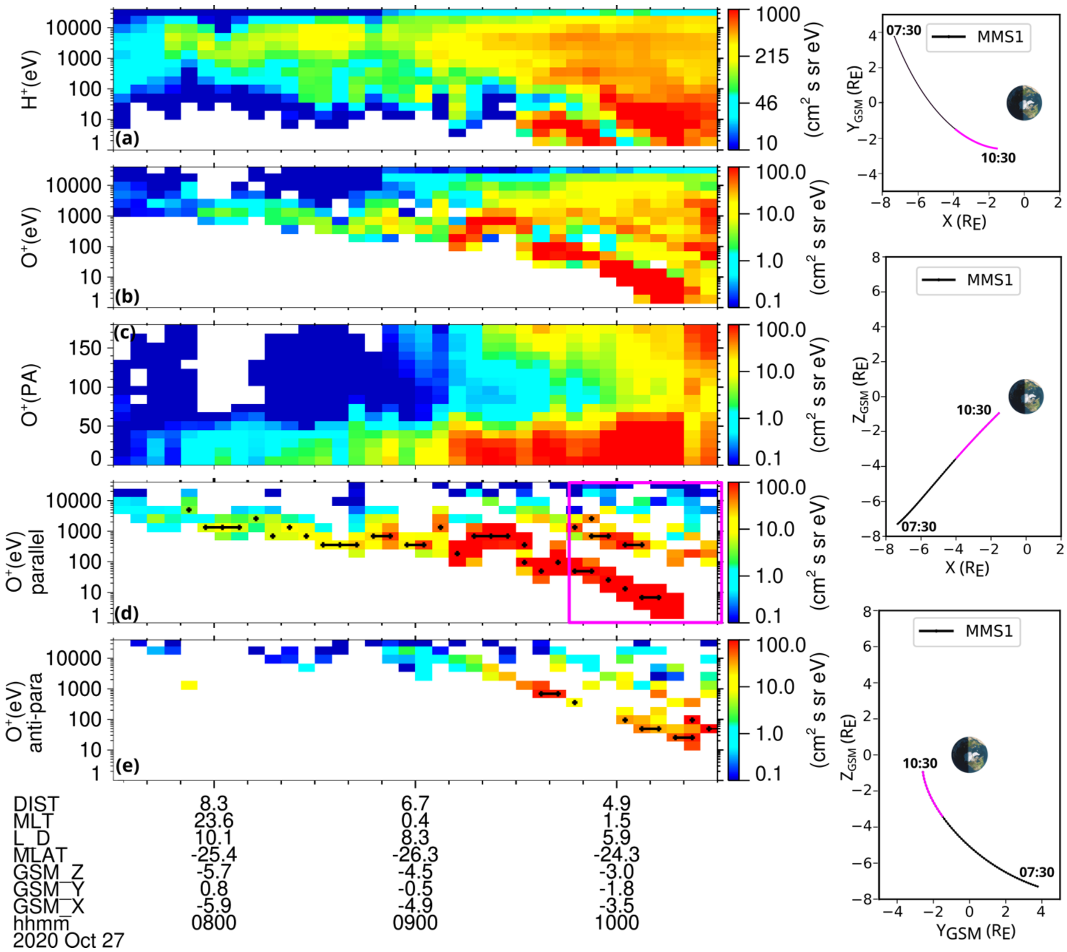

Figure 5. Observations of energetic streaming O^+ from the nightside auroral region. Panels from ton to down: Panel (a) is proton energy spectra over all angles. Panel (b) is O^+ energy spectra over all angles. Panel (c) is the pitch angle of O^+ at all energy. Panel (d) is the energy spectra of parallel O^+ with pitch angle between 0 and 60 degrees. Panel (e) is the energy spectra of antiparallel O^+ with pitch angle between 120 and 180 degrees. Black dots in panel (d) and panel (e) show the identified streaming O^+. MMS orbits are shown in projections of XY_{GSM}, XZ_{GSM} and YZ_{GSM} at the bottom of the figure.

3.2 Auto identification of streaming O^+ For MMS

The last panels of Figure 3, 4 and 5 show the results of the program we used to automatically identify streaming O^+. Previously, Liao et al. (2010) implemented a program to identify the streaming O^+ automatically using Cluster data. In this study, we are targeting a similar population but in different regions. First, as MMS is near/inside the PS, there can be more than one streaming population at different energies and directions. Second, we would like to identify the freshly outflowing populations, not a bouncing, bidirectional field-aligned population. Thus, we have modified the algorithm to accommodate the HPCA data collected at different regions covered by the MMS orbits. We start by averaging data for 5 minutes to increase the statistics of the data. We then separate data into parallel and antiparallel populations to capture streaming O^+ in both directions. For each direction, we calculated the pitch angle spectra for each energy bin and reviewed the pitch angle spectra to select the pitch angle distribution with a clear peak. To ensure the continuity of the streaming population, we require the streaming population to continue for more than three-time segments within the same or adjacent energy bin and pitch angle peaks. The result of the streaming O^+ identification is shown as the black marks in panel e and f of Figure 3 and 4, and panels d and e of Figure 5. More details of the identification algorithm can be found in Liao et al. 2010.

3.3 Database of streaming O^+

After running the identification program on MMS data from 2017 to 2020, we created a database with all the data observed within the magnetosphere (sheath and solar wind regions are taken out with the same methods recorded in Liao et al. 2011), with a flag indicating whether streaming O^+ is observed or not. The bidirectional streaming population is taken out, and only outflowing streaming O^+ is kept so we can study the outflow and transport of the streaming O^+ population. For the time periods when either parallel or antiparallel streaming O^+ is observed, the properties of the streaming O^+ are calculated (energy, flux, and density). Magnetosphere dynamic conditions (storm phases, Dst, and Kp index) and solar wind parameters (velocity, pressure, and IMF **B**) are recorded. Solar wind data are averaged over the 1 hour before the observation time of the streaming O^+.

4. The Transport Paths

4.1 Occurrence Frequency

Occurrence frequency is defined as the number of streaming O^+ events divided by the number of total observations in a particular location and under certain conditions. Occurrence frequency shows the probability that the streaming O^+ will be observed in a specific region. The sites with high frequency represent the transport path of O^+ within the energy range of the instrument. By studying the occurrence frequency maps in different magnetospheric regions under various solar wind conditions, we investigate how O^+ ions are transported and enter the plasma sheet.

4.2 Occurrence frequency Maps

Maps in Figure 6 are occurrence frequency maps of the streaming O^+, divided into different regions, and/or sorted by different conditions. We divided the planes into a 2 × 2 R_E grid and calculated the occurrence frequency of the streaming O^+ in each bin. The color represents the occurrence frequency with dark blue as 0% and red as 100%. To make sure there are enough statistics for the map, we require there to be more than 27 samples in each bin. The compression correction factor is applied.

The left group of maps in Figure 6 display the occurrence frequency of streaming O^+ in the XZ_{GSM} plane, for three ranges in Y_{GSM} (left to right: dawn, center, and dusk) and for different regions (top to down: lobe, PSBL, and PS). Overall, the streaming O^+ occurrence frequency decreases from the lobes, to the PSBL, to the plasma sheet. In Figure 6a-c, both south and north lobes are clearly identified, although there is no data coverage in the south-dawn lobe. The occurrence frequency is above 80% in both north-dawn, south-center, and south-dusk, with the highest frequency near the Z_{GSM} around+/-10 R_E. The high frequency regions are interpreted as the dominant transport path of the streaming O^+. The high frequency regions in Figure 6a-c match the observations in the (Liao et al. 2010). There is a clear asymmetry in Figure 6b and Figure 6c, with more frequent occurrence at south center and south dusk. This south-dusk preference of the streaming O^+ transport path is also discussed in (Liao et al., 2010). We will discuss the driver of the asymmetry in a later section. The consistency of the lobe observation with the previous study provides good validation of our methods.

The occurrence frequency maps in the PSBL shown in Figure 6d-f have higher frequency areas matching those in the lobe maps and a separate population at the near-Earth nightside region. On the duskside of the PSBL, as shown in Figure 6f, there is a high frequency region with occurrence frequency above ~70%, matching the transport path of streaming O^+ in the south dusk lobes, displaying straightforward evidence of the O^+ from the dayside cusp origin entering the PSBL. In the center PSBL, as shown in Figure 6e, the main part of the transport path is at the nightside around X = -10 R_E and Z_{GSM} between -5 R_E and 5 R_E, with occurrence frequency at ~80%. Part of the area overlaps with the streaming O^+ transport path in the southern lobe in Figure 6b. The rest does not have a matching area in the center lobes. One of the possibilities is that those ions are directly from the nightside auroral outflows. We will further discuss this population in the discussion. On the dawnside of the PSBL, as shown in Figure 6d, the overall occurrence frequency is around 50%. There is a slightly higher rate region at the outer northern tail, matching the high frequency area in the dawnside lobe in Figure 6a, so this region could be the location where streaming O^+ enters the PSBL from the lobes. There are also high rates observed in the southern near-Earth region.

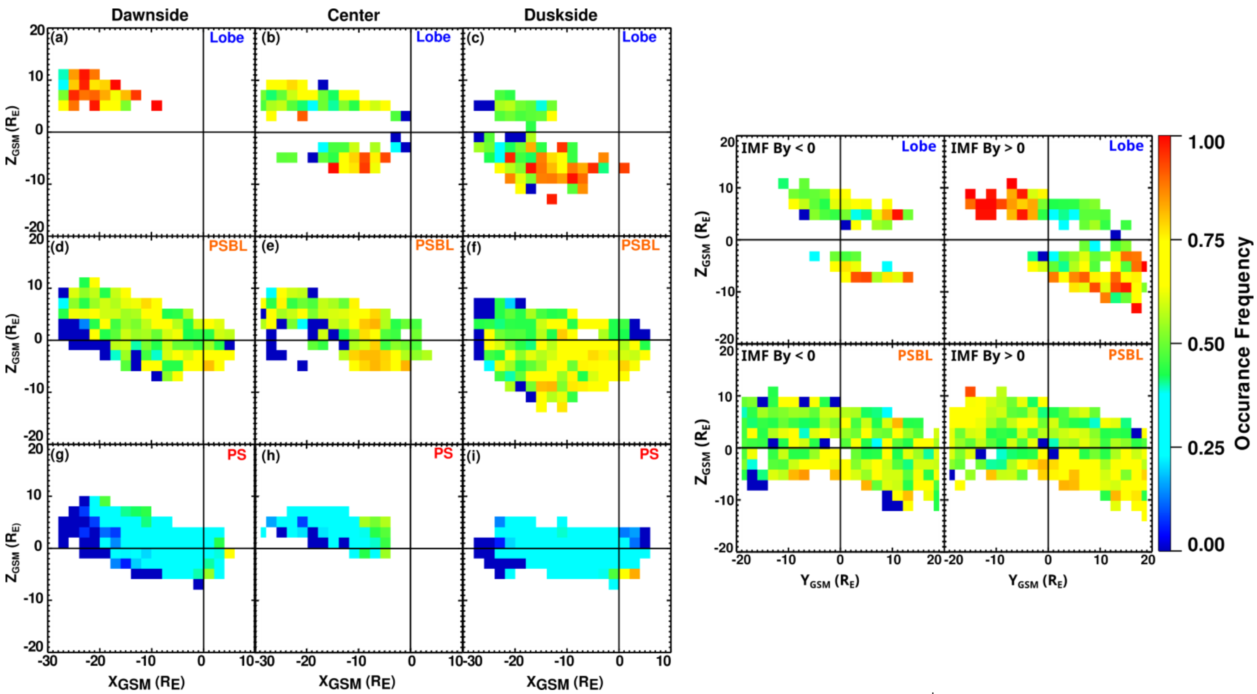

Figure 6. On the left are the occurrence frequency maps of streaming O^+ in the XZ_{GSM} plane, for different Y_{GSM} ranges (from left to right: dawn -20 R_E > Y_{GSM} > -5 R_E, center -5 R_E < Y_{GSM} < 5 R_E and dusk 5 R_E < Y_{GSM} < 20 R_E), and different regions (from top to down: lobe, plasma sheet boundary layer and plasma sheet). On the right are the Occurrence frequency maps of streaming O^+ in YZ_{GSM} plane, sorted by IMF B_Y (left column is for IMF B_Y < 0; right column is for IMF B_Y > 0), and regions (top: lobe; down: plasma sheet boundary layer). The color represents the occurrence frequency with dark blue as 0% and red as 100%. Correction factors for the compression have been applied.

In the plasma sheet, the overall occurrence frequency of the streaming O^+ is the lowest (~27%), as shown in the last row on the left side of Figure 6. It indicates that O^+ streaming in the lobes, passing through PSBL, and entering the plasmasheet are scattered as they enter the high-density region, become isotropic, and can no longer be identified as a beam. The occurrence frequency is flat at most locations, indicating that the entry of streaming O^+ happens at all locations of PSBL. Some areas near the Earth reach a higher occurrence rate at ~50%. This near-

Earth streaming O^+ is likely the low energy O^+ entry directly from the nightside auroral region into the plasma sheet.

4.3 Asymmetry of the transport paths maps

Liao et al., 2010 discovered a similar asymmetry in the transport of the streaming O^+ from the cusp source and identified IMF By as the main driver of the asymmetry, along with the convection patterns at the source region. To compare the drivers of the asymmetric transport path observed by MMS in different regions with the Cluster results, we sort data into positive and negative IMF By and plot the lobe and PSBL occurrence frequency maps in YZ_{GSM} projection, as shown on the right side of Figure 6. When IMF By is positive, streaming O^+ travels preferentially at the north-dawn and south-dusk sides in the lobes and PSBL. When IMF By is negative, no noticeable asymmetry is observed. There is no asymmetry observed in the plasma sheet regardless of the direction of IMF By (not graphed). This result agrees with the previous study of the transport path of O^+ steaming from the dayside cusp using Cluster data (Liao et al., 2010).

4.4 Transport path of O^+ by energies

The velocity filter effect separates the different energies of streaming ions. To better study energization and identify the sources of the streaming O^+, we plot the occurrence frequency maps (row (a)-(c)) and density maps (row (d)-(f)) of streaming O^+ in XY_{GSM} at different energy ranges and in different regions in Figure 7. The color bar for occurrence frequency is from 0-0.6. The orbits of MMS are near the equatorial plane with most of the data collected with Z_{GSM} less than 10RE. The arrangement of the maps is the same in both sets of maps: column left to right: < 100 eV, 100 - 1000 eV, 1-3 keV, and > 3 keV, and rows top to bottom: lobe, PSBL, PS. The denominators (total number of observations in a bin) of the occurrence frequency are the same for all energy maps in the same region. The compression correction factor is applied. The density is calculated for all the observed streaming O^+ in each grid. The compression scheme has minimal effect on the density maps because the streaming O^+

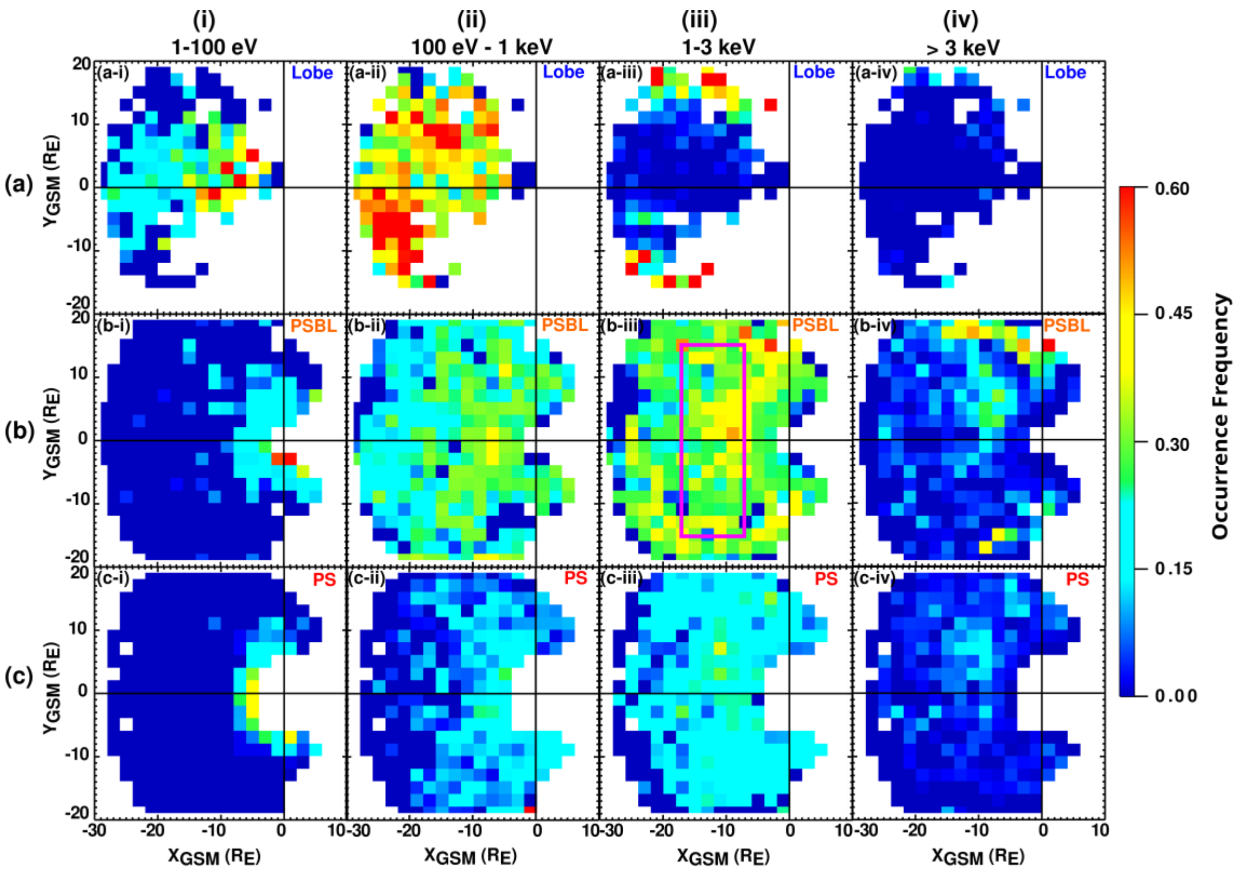
(i)
1-100 eV
(ii)
100 eV - 1 keV
(iii)
1-3 keV
(iv)
> 3 keV
(a)
(b)
(c)
Lobe
PSBL
PS
YGSM (RE)
XGSM (RE)
Occurrence Frequency
0.60
0.45
0.30
0.15
0.00

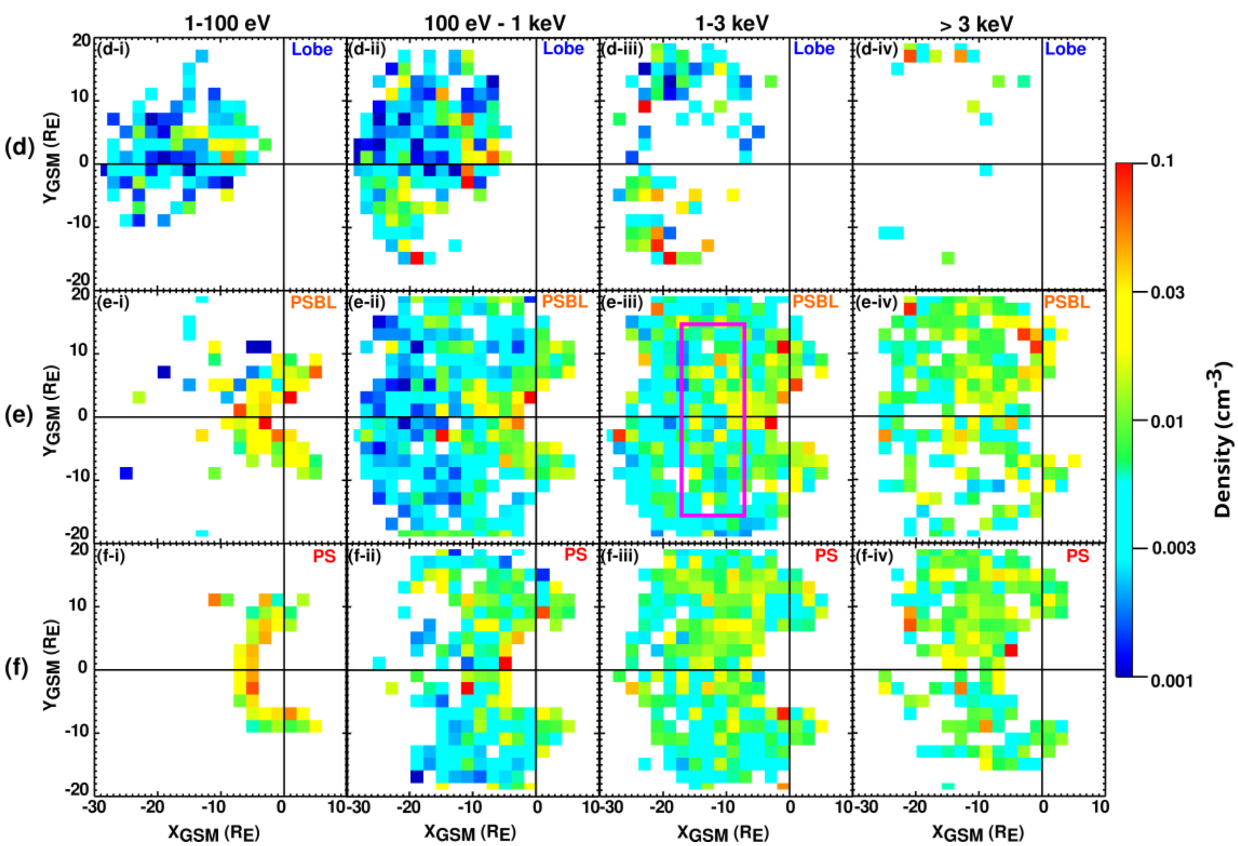
1-100 eV
100 eV - 1 keV
1-3 keV
> 3 keV
(d)
(e)
(f)
Lobe
PSBL
PS
YGSM (RE)
XGSM (RE)
Density (cm-3)
0.1
0.03
0.01
0.003
0.001

424

Figure 7. Occurrence frequency and density 7-maps of streaming O^+ for different energy ranges (left to right: 1eV ~ 100 eV, 100eV ~ 1keV, 1 keV ~ 3 keV, > 3 keV) and in different regions (top to down: lobe, plasma sheet boundary layer and plasma sheet). Correction factors for the compression are applied for the occurrence frequency maps. Pink shapes are areas for fluence estimation in section 7.

is strongly anisotropic, concentrated in relatively few angular bins. The comparisons between density maps before and after compression are in Appendix A.

The row (a) and row (d) of Figure 7 display the occurrence frequency and density maps of streaming O^+ in the lobes. The streaming O^+ with low energy (< 100 eV) travels near the center of Y_{GSM} and can reach as far as -28 R_E, as shown in panel (a-i). It is possible that due to the variation of the convection field strength, which drives traveling distance of the outflowing O^+ in the lobe, the low energy lobe streaming O^+ can travel and arrive at different distances. The density of this population, as shown in panel (d-i), is slightly higher near the Earth and lower in the outer area, resulting from the different magnetic field strengths near the Earth and further down the tail. The highest occurrence frequency in the lobes is observed in Figure 7(a-ii), the map for streaming O^+ from 100 eV to 1 keV, with the highest rate on the dawnside close to the flank. The asymmetry is driven by the IMF By as discussed earlier. Figure 7(a-iii) shows that streaming O^+ from 1 to 3 keV are seen mostly near the dawn and dusk flanks. The number densities of lobe streaming O^+ at higher energy ranges, as in panel (d-ii) and panel (d-iii), are similar (~0.005 cm^{-3}) to the ones in lower energy, except on the dawnside where density can reach 0.01 cm^{-3}.

As discussed in the previous section, this dawnside lobe population is in the northern hemisphere and driven by positive IMF By. There are limited observations of streaming O^+ above 3 keV in Figure 7(a-iv), and they are mostly concentrated near the flanks as well. Overall, in the lobes, streaming O^+ ions outflowing from the dayside spread across all HPCA energy ranges, with slower ions observed near the center of Y_{GSM} and faster ions traveling closer to the dawn and dusk flanks. They can reach the as far as the MMS orbits covers in the tail direction and Y_{GSM} direction. Noting that the Z_{GSM} coverage is within +/-10R_E. There may be more energetic populations outside the satellite orbit. The density of cusp outflowing population is roughly from 0.005 cm^{-3} to 0.01 cm^{-3} across energy ranges.

Inside the PSBL, almost all low-energy streaming O^+ ions are near the Earth, with an occurrence frequency of ~18%. The transport path of the slow streaming O^+ in the PSBL, as shown in Figure 7(b-i), is quite different from the one in the lobes, as shown in Figure 7(a-i). Their density, as shown in Figure 7(e-i), is around 0.02 cm-3, much higher than the density of lobe streaming O^+ in Figure 7(d-i). The difference suggests that the observed low-energy outflowing O^+ in the PSBL are not from the lobes, i.e., not originated from the dayside cusps. Their spatial distribution and observed regions are consistent with direct outflow from the nightside auroral. While this population is not clear in the occurrence frequency maps for higher energy O^+ in PSBL in Figure 7(b-ii) and (b-iii), we do witness a high-density (~0.01 cm^{-3}) population located at the similar near-Earth area in Figure 7(e-ii) and in Figure 7(e-iii). This is consistent with the event shown in in Figure 5: streaming O^+ ions outflowing from the auroral oval cover a wide range of energies.

Streaming O^+ ions in the PSBL from 100 eV to 1 keV are observed over the whole region, with occurrence rates from ~15% to ~30% as shown in Figure 7(b-ii). Figure 7(e-ii) plots the density map for this population: the density is at ~0.003 cm^{-3} in most areas and there is a high-density region near the Earth. The similarity between the density range in outer area in Figure 7(e-ii) and the of lobe streaming O^+ suggests that those PSBL streaming O^+ has a lobe source. The low-energy streaming O^+ in the lobes is likely accelerated during the entry into the PSBL and become more energetic and observed at higher energy range as streaming O^+ from 100 eV to 1 keV moving in the PSBL. This is consistent with the case study in Figure 3: the energy gradually increases when entering from the lobe into the PSBL. The high-density region near the Earth is at a similar location as those of low-energy PSBL streaming O^+ in Figure 7(b-i) and Figure 7(e-i), indicating that they are from the same nightside auroral source.

The highest PSBL occurrence frequency is observed in Figure 7(b-iii), the map of streaming O^+ from 1 to 3 keV. Because lobe streaming O^+ at this energy range are mostly found near the mantle area, the observed PSBL energetic streaming O^+ (1-3 keV) are most like from the combination of the entry of the lower-energy ions in the lobe, and direct outflow from the nightside auroral regions. O^+ ions streaming in the lobe are heated and accelerated as they enter the PSBL. The area of high occurrence rate (yellow) near the (-10 R_E, 0 R_E) in the PSBL maps for O^+ from 1 to 3 keV, as shown in Figure 7(e-iii), points out the location where auroral outflowing O^+ enters the PSBL directly along the closed field lines. The density of energetic streaming O^+ at 1-3 keV, as shown in Figure 7(e-iii), is overall higher than the less energetic O^+, supporting the population observed in Figure 7(e-iii) a highly mixed from both sources.

In Figure 7(b-iv), there are highly energetic (> 3 keV) streaming O^+ observed at the duskside. The duskside asymmetry may be due to the tilt of the orbits leading to a lack of data on the south-dawn side of the magnetosphere, which is evident in Figure 6. This duskside observation, as in Figure 7(e-iv), has a density (~0.02 cm^{-3}) between the regular lobe entry O^+ (~0.004 cm^{-3}), and the auroral entry observed near the Earth (~0.01 cm^{-3}), which again suggests a mixed sources. Moreover, the near-Earth population that is evident in Figure 7(e-i) and Figure 7(e-ii) for streaming O^+ lower than 1 keV is not as clear in Figure 7(e-iii) and not seen in Figure 7(e-iv), indicating the more energetic streaming O^+ from the nightside auroral source can travel further out in the PSBL.

Overall, in the PSBL maps, we observed the streaming O^+ from the dayside cusps and the direct entry of nightside auroral outflow. Low energy O^+ from the lobes are accelerated during the entry and observed at higher energy inside the PSBL. Streaming O^+ from the nightside auroral sources are at wide energy ranges, with lower energy population closer to the Earth and more energetic O^+ observed further out.

For streaming O^+ inside the plasma sheet, the occurrence frequency (< 20%) is lower than in the PSBL in general, as shown in the 3rd row in Figure 7, except for streaming O^+ lower than 100 eV. The decrease of occurrence frequency from the lobes to the PSBL and then PS is likely due to the streaming O^+ ions scattered and becoming more isotropic as they enter a denser region. The density of streaming O^+ in the plasma sheet averages around 0.01 cm^{-3}. As shown in Figure 7(c-i) and Figure 7(f-i), streaming O^+ ions with low energies are found near the Earth, with similar location and density as the observation in the PSBL (but not seen in the lobe map), showing auroral outflowing O^+ streaming in the PSBL enter the plasma sheet, which can then feed the ring current. For streaming O^+ from 100 eV to 1 keV in the PS, as shown in Figure 7(c-ii), they are generally spread across the tail with an occurrence frequency of ~10%, except near the tail and Y_{GSM} central region. The density pattern for PS streaming O^+ at the same energy range, as shown in Figure 7(f-ii), is similar to the PSBL density map. The missing population seems to be the low-density lobe entry population. One possible explanation is that because this region is where the magnetic field is more stretched and less dipole-like, ions are more likely to be scattered and less beam-like, and hence not detected as streaming population. Another possibility is that those PSBL streaming population are accelerated and heated during entry, so they are not now categorized into higher energy maps. In Figure 7(c-iii), the occurrence frequency is flat at ~20% for streaming O^+ from 1-3 keV. In the corresponding density map in Figure 7(f-iii), there is a duskside preferences, which is weak but exist in the PSBL density map in Figure 7(e-iii). For streaming O^+ above 3 keV inside the PS, the asymmetry in the occurrence frequency map (Figure 7(c-iv)) is likely inherited from the PSBL, consistent with streaming O^+ entering the PS from the PSBL, and partially due to the uneven orbit coverage of MMS.

5. Energy Maps

We further studied the energy distribution of the streaming O^+ to understand how outflowing O^+ with different energies behaves in the magnetosphere. We created median and minimum energy maps in different regions to assess how the energy profile changes during transport and entry into the plasma sheet. Figure 8 displays the median and minimum energy maps in XY_{GSM} for the lobe, PSBL, and PS.

5.1 Median Energy Maps

The median energy is lowest in the lobe (averaged at 591 eV), higher in PSBL (averaged at 1409 eV), and highest in PS (averaged at 1750 eV). Within the lobes, the median energy increases gradually as Y_{GSM} increases, i.e., low-energy O^+ is observed in the center while energetic ions are observed further out in the Y_{GSM} direction. While the velocity filter effect should play a key role in this pattern, this energy pattern indicates limited energy dependence of streaming O^+ on X.

In the PSBL, a weak radial dependence is observed, with the lowest energy (~100 eV) observed on nightside near the Earth, and the highest observed further down the tail (~300 eV to ~3 keV). There is a slight tendency for the highest energy O^+ to be observed near the flank area (large Y_{GSM}), and an asymmetry with more energetic O^+ observed on the duskside of the PSBL. Comparing with the maps in the row (e) of Figure 7, the near-Earth population with energy lower than 300 eV are the streaming O^+ from the nightside auroral oval while the more energetic population at outer area are populations mixed from the accelerated O^+ from the lobe and energic part of auroral outflows.

Inside the plasma sheet, the averaged energy is the highest among all three regions. We can still observe the low-energy O^+ streaming near the Earth but with greater energy than those observed in the PSBL. In most parts of the plasma sheet, the energy is greater than 1 keV. Again, the low-energy population is likely to be from the nightside auroral region while the energetic population is from mixed sources. There is an asymmetry with higher energy ions observed on the duskside, which is consistent with the observation in Figure 7(c-iv) and figure 7(f-iv).

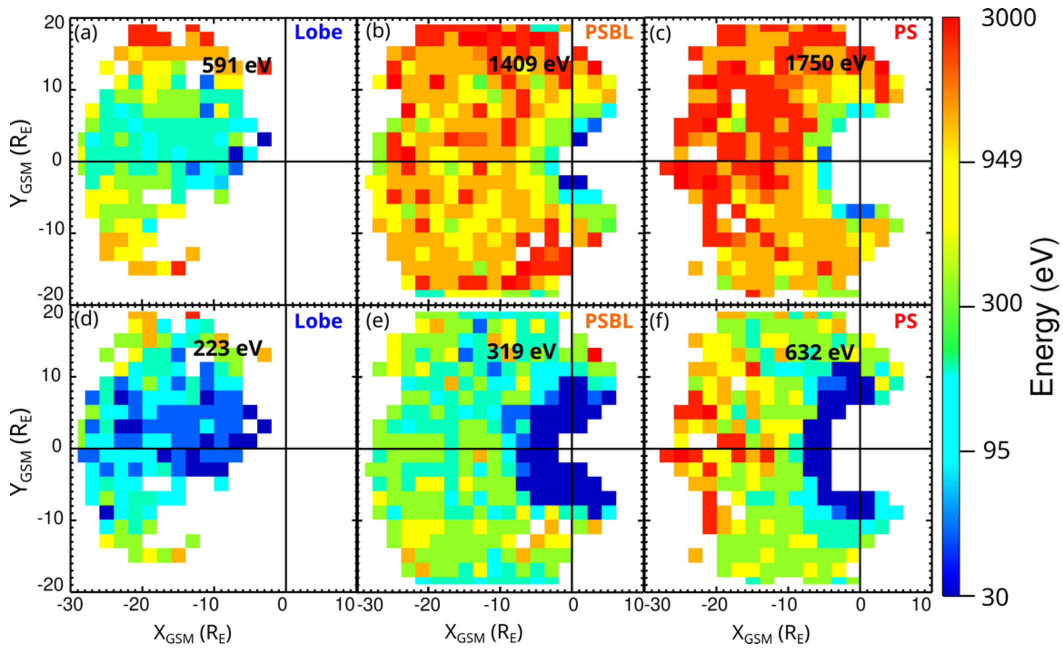

Figure 8. Median (top row) and minimum (bottom row) energy maps of streaming O^+ in XY_{GSM} projections in different regions (left to right: lobe, plasma sheet boundary layer and plasma sheet).

5.2 Minimum Energy Maps

The 2nd row Figure 8 plots the minimum energy maps of streaming O^+ in the XY_{GSM} plane. Each grid point shows the lowest energy of all the identified streaming O^+ events at each location. The minimum energy map shows where the low-energy O^+ cannot reach.

Like the median energy maps, the minimum energy is generally increasing with the plasma beta. In the lobes, the minimum energy is the lowest at the center of Y_{GSM} and increases gradually towards the flanks. Most of the low energy O^+ (< 30 eV) are constrained near the Earth and do not make it far down to the tail, as expected for the velocity filter effect. Streaming O^+ less than 80 eV mostly streaming near the center of Y_{GSM}, does not reach area with the large Y_{GSM}.

As in the median energy map in the PSBL, two distinct populations are observed in the PSBL minimum energy maps: the population with low energy (< 30 eV) and only observed near the Earth, and the population further out, with similar minimum energy range around 300 eV. It is consistent with velocity filter effect that slow outflowing ions reach the plasmasheet closer to the Earth not further down the tail.

A similar trend is observed in the PS. The streaming O^+ ions with the lowest energy are only observed near the Earth, and the minimum energy of streaming O^+ in the outer areas are much higher. The overall energy is higher in the PS than the observed ones in the PSBL, implying either acceleration occurred during O^+ entry from the PSBL into the PS, and/or less energetic streaming O^+ ions are easier to be scattered and lose their streaming features when they enter the plasma sheet.

At the center of Y_{GSM} and X < -10 R_E, there is an area where the lowest energy observed is above 700 eV. This is consistent with Figure 7(c-ii): the streaming O^+ lower than 1 keV is not observed in the center in Y_{GSM}. By comparing this with Figure 7(c-ii), one can see that this increase in minimum energy is due to the lack of low energy population in this area. The more stretched magnetic field in this area that efficiently in scattering the streaming population may be the cause of this.

6 The Impact of Geomagnetic Activity and Solar Wind Drivers

6.1 Kp Index

Because the data collection time covers the end of the declining phase of solar cycle 24, there are only a few magnetic storms during 2017-2020. As a result, we have limited storm time data to study the storm phase impact on the maps of streaming O^+, and so we use the more general Kp index to study activity dependence. To investigate how the geomagnetic activity influences the transport and the entry, we plot, in Figure 9, the streaming O^+ maps in occurrence frequency, density, median and minimum energy, sorted into two Kp ranges: Kp < 2 and Kp >= 2, in different regions.

Inside the lobe (the two left columns in Figure 9), the occurrence frequency, density, median and minimum energy increase when KP index is higher, as shown in the 2nd column in Figure 9). It implies a more frequent, stronger and more energetic O^+ outflows from the dayside cusp source during more active time.

The middle two columns in Figure 9 display the Kp index impact on the PSBL streaming O^+. When Kp index is higher, the occurrence rate is clearly higher for both the near-Earth population and the O^+ entering at larger distance. Similar increases can be seen in the density map, indicating a more intense O^+ population in the PSBL during non-quiet time. There are also increases in the median energy maps, which may be the result of a stronger acceleration or a shift on the energy distribution of the outflowing O^+ when Kp index is higher. The increase in the minimum energy map is evident but not as strong, which may be because it is the minimum convection that drives the minimum energy maps. The streaming O^+ from the auroral sources, identified as the low-energy high-density population observed at the inner-edge of the plasma sheet, is clearly enhanced and more energetic during active times. Because the O^+ from the dayside cusp source is mixed with energetic O^+ from the auroral sources at the larger distance, there is no direct evidence for the enhancement of lobe source O^+ in the PSBL. However, it is expected that due to the stronger outflow, the more dynamic magnetosphere is likely to bring more lobe O^+ into the PSBL.

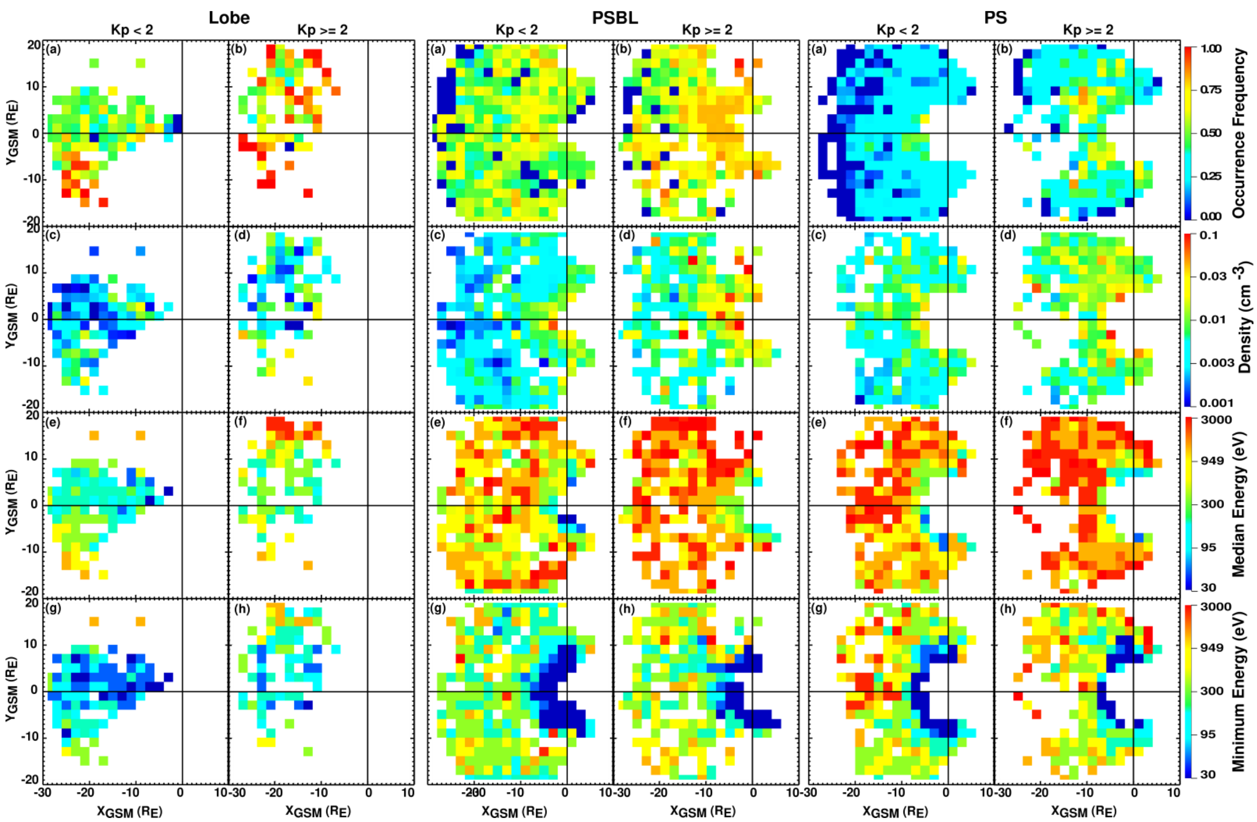

Figure 9. Maps of, from top to down, occurrence frequency, median density, median energy, and minimum energy, divided into different regions (lobe, plasma sheet boundary layer and plasma sheet), and sorted by KP index (for each region, left column: KP >= 2, right column: KP < 2). Correction factors for the compression have been applied to the occurrence frequency maps.

The right two columns in Figure 9 show how streaming O^+ inside the plasma sheet changes for different Kp ranges. When KP is higher, the streaming O^+ ions in the plasma sheet are more frequently observed, and their density is also higher, showing a stronger and more frequent input of streaming O^+ into the plasma sheet, forming a more populated plasma sheet. The increase in the plasma sheet median energy map shows the O^+ entering the plasma sheet is more energetic when the magnetosphere is more active. There is a slight increase in the minimum energy map.

Figure 9 showed how streaming O^+ in different regions reacts to a more active magnetosphere. It confirms that higher activity correlates with more frequent and stronger O^+ outflow from the dayside cusp and night auroral region, leading to a more frequent, stronger and more energetic O^+ input into the plasma sheet, which can lead to a stronger ring current during storms.

6.2 Solar Wind Drivers

As mentioned in the last section, 2017-2020 is in the declining phase of solar cycle 24 and the F10.7 is below 100 sfu the whole time. The solar wind velocity drives the dawn-dusk convection field, which generates an E×B convection that brings the ions from the cusp tailward and towards the central plasma sheet. Thus, the solar wind velocity is expected to have a strong impact on the transport path of the ions. Figure 10 shows maps of, from top to bottom, occurrence frequency, density, median, and minimum energy, sorted by solar wind velocity (top group) and solar wind pressure (bottom group) in PSBL and PS. Because solar wind has impacts on the ion transport from the source to the observed location, the value used for the map is the solar wind parameters averaged over 1 hour before the observation time. The 1st column on the left shows the streaming O^+ observed when solar wind velocity is less than 400 km/s, and the 2nd column shows those observed when solar wind velocity is greater than 450 km/s. The 3rd and 4th columns show the streaming O^+ observed when solar wind pressure is below and above 2 nPa.

Comparing the 1st and 2nd columns in the top 4 rows, we confirmed that the solar wind velocity indeed has a significant impact on the streaming O^+ in the PSBL. Higher solar wind velocity leads to higher occurrence frequency at all locations, especially for streaming O^+ originating from auroral regions observed near the Earth. Similarly, the increase of the density under faster solar wind condition is evident, and the increase is stronger for the population with larger distance from the Earth. There is a significant jump in the median energy at most of the locations. This trend is consistent with the direct impact on the ion transport path: faster solar wind leads to a much stronger convection force that brings more energetic ions down towards the

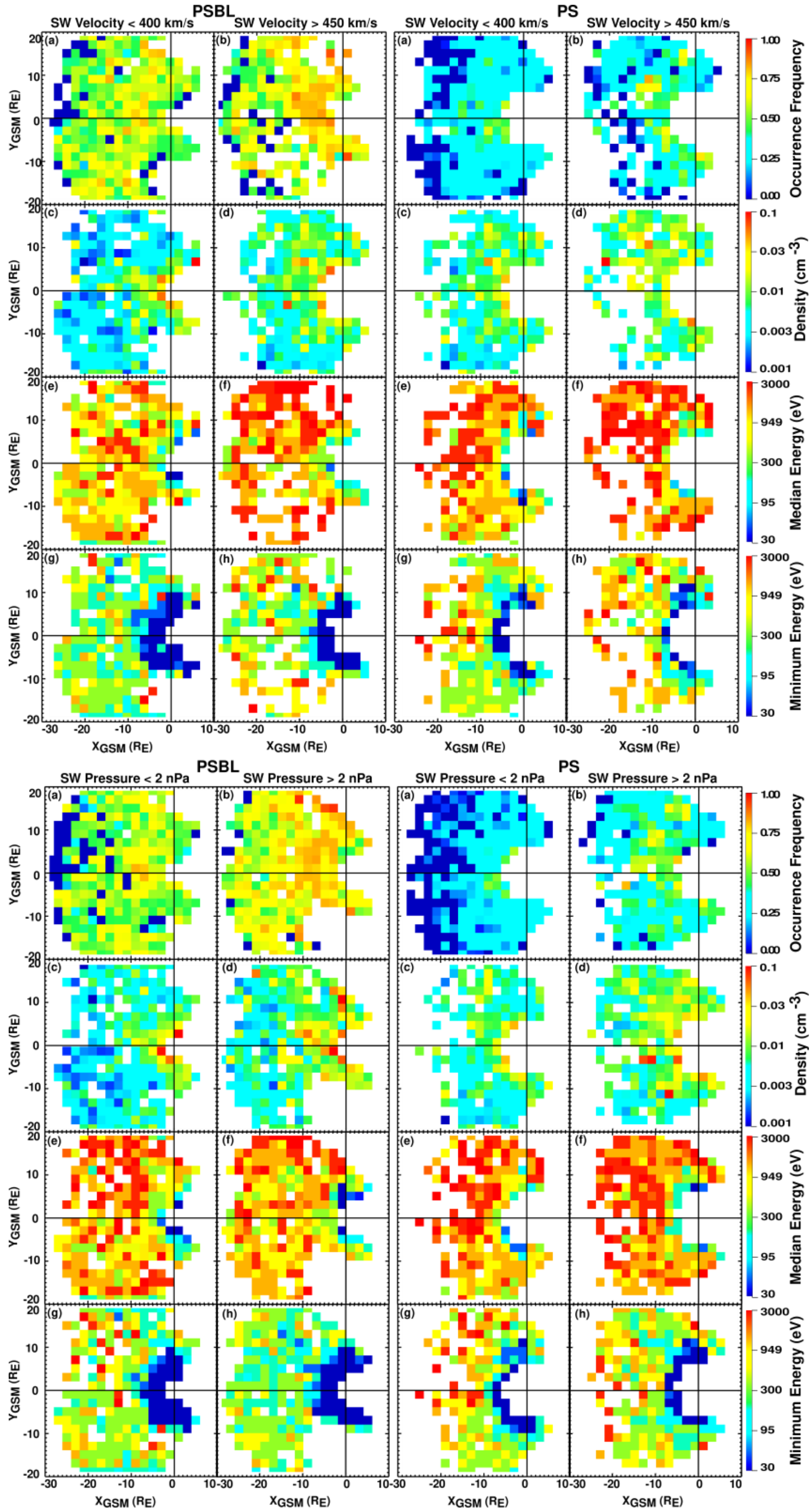
PSBL
SW Velocity < 400 km/s
SW Velocity > 450 km/s
PS
SW Velocity < 400 km/s
SW Velocity > 450 km/s
Occurrence Frequency
Density (cm -3)
Median Energy (eV)
Minimum Energy (eV)
YGSM (RE)
XGSM (RE)
PSBL
SW Pressure < 2 nPa
SW Pressure > 2 nPa
PS
SW Pressure < 2 nPa
SW Pressure > 2 nPa
Occurrence Frequency
Density (cm -3)
Median Energy (eV)
Minimum Energy (eV)
YGSM (RE)
XGSM (RE)

Figure 10. Maps of, from top to down, occurrence frequency, median density, median energy, and minimum energy, divided into different regions (PSBL and plasma sheet), sorted by solar wind velocity on the top (V_{SW} < 400 km/s and V_{SW} > 450 km/s), and sorted by solar wind pressure on the bottom (P_{SW} >= 2 nPa and P_{SW} < 2 nPa). Correction factors for the compression have been applied to the occurrence frequency maps.

neutral sheet at a much closer distance. Similarly, stronger convection brings the low-energy ions into the PS near the Earth, so there are no low-energy streaming O^+ ions observed further out. This explains the increase of the minimum energy at a given distance under fast solar wind. A similar trend is seen for the plasma sheet by comparing the 3rd and 4th column of the top 4 rows in Figure 10.

The bottom 4 rows of Figure 10 show the impact of the solar wind pressure. The 1st and 2nd columns show streaming O^+ observed when solar wind pressure is less than and greater than 2 nPa in the PSBL. The occurrence frequency increases at most of the locations when solar wind pressure is higher, showing a stronger and more frequent O^+ entering the PSBL under high solar wind pressure. The density also increases under enhanced solar wind pressure, which may be due to both strong solar wind pressure compressing the magnetosphere and/or increasing outflows. The changes in the median and minimum energy maps are not significant. Similar trends are found also in the plasma sheet that enhancement of O^+ entry is observed when solar wind pressure higher, but the energy patterns stay the same, which suggests that the energy profiles are highly dependent on the convection field, which is less correlated with the solar wind pressure than solar wind velocity.

7. Discussion

7.1 Streaming O^+ origin and transport path

The occurrence frequency and density maps in Figure 7, and the energy maps in Figure 8 present the distribution of the streaming O^+ in the magnetosphere and their density and energy profiles. As discussed earlier, there are three distinct populations.

The streaming O^+ ions from the dayside cusps are traveling in the lobes with widespread energy ranges (< 3 keV) and locations. The spatial distributions show an energy dependence on Y_{GSM}: slower O^+ ions traveling in the center of Y_{GSM} and more energetic ions traveling near the larger Y_{GSM}. Seki et al. (2000) have previously reported similar streaming O^+ with high energy observed in the lobe/mantle area with large Y_{GSM}. This energy pattern is lost once the population enters the PSBL. The energetic O^+ above 3 keV may reach the flanks outside Y_{GSM} = 20 R_E, and leak into the magnetosheath. Their transport path has an IMF By driven asymmetry that preferentially travels on the north-dawn and south-dusk sectors. They can enter the PSBL at all locations with acceleration that brings all of them above 100 eV. The streaming O^+ has an average density of ~0.005 cm^{-3} in the lobes, and the density increases in the PSBL, and becomes even higher as they enter the plasma sheet. This population becomes more frequent, more intense and more energetic when the magnetosphere becomes more active. Stronger solar wind brings more dayside cusp origin O^+ into the plasma sheet.

Streaming O^+ ions close to the earth are observed in the PSBL, and then convect into the plasma sheet. Their median energy is very low (~30 eV), but the energy range extends to the keV range (< 3 keV). The median density is high, above 0.02 $cm^{-3,}$ inside the PSBL and plasma sheet. They are more frequent and intense when the solar wind velocity is above 450 km/s, and the convection field is strong. They are likely to be from the nightside auroral region.

There is a third high-energy and high-density population observed at the south-dusk side of the PSBL and the PS. It is the main contribution to streaming O^+ above 3 keV inside the PSBL and the plasma sheet. It is different from the lobe entry population due to its high density and much higher energy. The dusk preference of this population may be due to the asymmetry of the MMS orbits that lead to a limited coverage at south-dawn section. The median density of this population (~0.01 cm^{-3}) is between the typical lobe density (~0.005 cm^{-3}) and the density of the near-Earth dense population (~0.02 cm^{-3}), suggesting this population may be a mixture of streaming O^+ from different sources. It likely contains the energetic portion of the nightside auroral outflows, which are from the same source as the inner edge low-energy high-density population but travel further down the tail due to the energy of the ions, as shown in Figure 1.

7.2 The contribution of streaming O^+ to the Plasma Sheet population

To investigate how the streaming O^+ from various sources impacts the composition of the near-Earth plasma sheet from 6 R_E to 15 R_E, we need to estimate the entry and loss of ions inside a plasma sheet. To achieve that, we make a simplifying assumption that the plasma sheet is a rectangular slab, as shown in Figure 11, with X between (-7 R_E, -17 R_E), Y between (-15 R_E, 15 R_E), and Z between (-2 R_E, 2 R_E) and that for "average" (mainly quiet) times, there is a steady state, so that the inflow should equal the outflow. We then examine the inputs and the outputs of the plasma sheet to study the contributions of various sources. The choices of 7 R_E and 17 R_E are based on available data extracted from various references. We assume the net flow in the cross-tail direction is zero, that is, the same number of ions drifting in from the dawnside are drifting out on the dusk side. We note that the extracted values are based on average values, so the estimation is for quiet time. During active times, the density and convection velocity are expected to be higher.

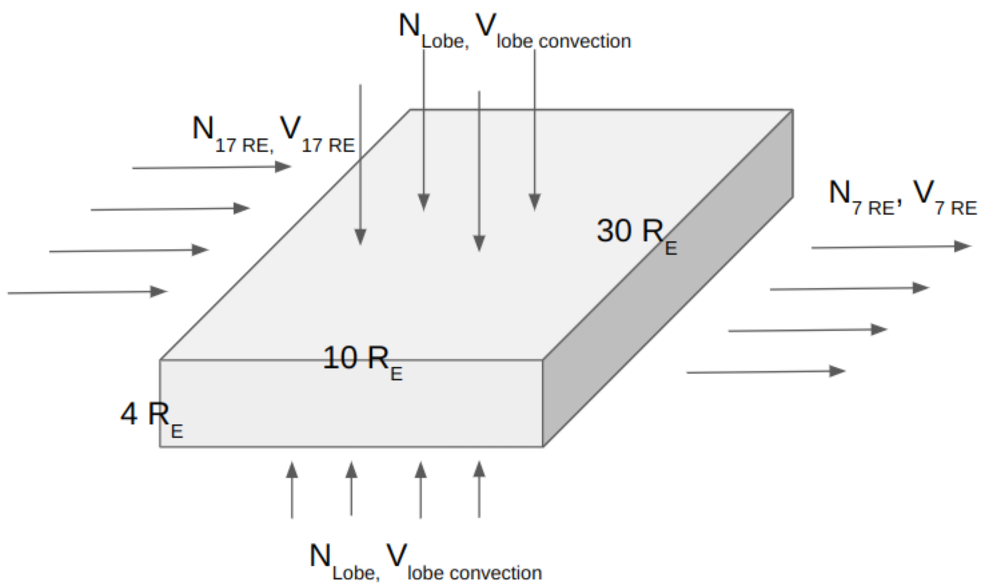

Figure 11. Schematic graph showing the slab model of plasma sheet with ions streaming in from magnetotail, lobes and out from the plasma sheet. The dimensions are X: [-7 R_E, -17 R_E], Y: [-15 R_E, 15 R_E], Z: [-2 R_E, 2 R_E].

There are three known sources that contribute to the main composition of the plasma sheet from 7 R_E to 17 R_E: the streaming O^+ entering from the north and south lobes, the streaming O^+ enter from the nightside auroral region, and the more distant plasma sheet convecting Earthward at 17 R_E. The loss, or output from the plasma sheet is the Earthward convection of ions at 7 R_E into the inner magnetosphere. To estimate the input and output of the plasma sheet, we need to calculate the fluence, the number of ions per second flowing through an area. The fluence is the product of the number flux and the size of the area, and the number flux can be calculated by multiplying the plasma density and the convection velocity. To estimate the fluence of H^+ and O^+ from the lobes, we multiply the ion density inside the lobes by the convection velocity perpendicular to the plasma sheet, the occurrence frequency and the area of both north and south lobes (10 R_E × 30 R_E × 2). The input from the tail plasma sheet is the product of ion density at 17 R_E plasma sheet, the inward convection velocity at 17 R_E and the area of the cross-section of the plasma sheet (10 $R_E \times 4 R_E$), as shown in Figure 11. The output to the inner magnetosphere is calculated by multiplying the plasma sheet ion density at 7 R_E by the inward convection velocity at 7 R_E and the cross-section of the plasma sheet at 10 $R_E \times 4 R_E$.

Ion Specie	F10.7	Flow Type	Measurement	Reference	occurrence rate
H^+ Density (cm^{-3})	> 100	Lobe input	0.14 (0.06~0.24)	Engwall et al. 2008	68%
	All	Tail Input	0.27 (0.21~0.32)	Maggiolo & Kistler 2014	
	All	Auroral Input	Unknown		
	All	Output	0.86 (0.82~0.92)	Maggiolo & Kistler 2014	
O^+ Density (cm^{-3})	< 100	Lobe input	0.004 (0.003~0.006)	This study	63% (50%~76%)
		Tail input	0.005 (0.005~0.005)	Maggiolo & Kistler 2014	
		PSBL Observation	0.005 (0.004~0.008)	This study	60% (53%~68%)
		Output	0.064 (0.05~0.078)	Maggiolo & Kistler 2014	
	> 100	Lobe input	0.009 (0.004~0.023)	Liao$^+$ 2011 (majority > 100)	66%
		Tail input	0.011 (0.003~0.028)	Maggiolo & Kistler 2014	
		Auroral Input	Unknown		
		Output	0.17 (0.14~0.19)	Maggiolo & Kistler 2014	
Convection Velocity (km/s)	All	Lobe input	7.55 (7.0~8.1)	Haaland$^+$ 2008	
		Tail Input	22.5 (18.3~26.6)	Chong$^+$ 2021	
		Output	13.0 (7.48~18.6)	Chong$^+$ 2021	
	< 100	PSBL Observation	38.9 (33.4~46.1)	This study	

Table 1. Median and quartile value of data extracted and aggregated from references and data from this statistical study with MMS/HPCA data.

We extracted density and convection velocity data from a number of studies (Engwall et al., 2008; Haaland et al., 2008; Liao et al., 2011; Maggiolo & Kistler et al., 2014; Chong et al., 2021) and cross checked the number with others (Angelopoulos et al., 1993; Juusola et al., 2011a; Juusola et al., 2011b; Miyashita et al., 2020; Chen et al., 2007; Kistler & Mouikis , 2016;

Mouikis et al., 2010). Table 1 shows the extracted and aggregated data and the references it was extracted from. The result of the fluence estimation is shown in Table 2.

As the O^+ from both dayside and nightside sources are mixed inside the PSBL, to estimate the fluence of O^+ from the nightside auroral outflows, we can calculate the total fluence of streaming O^+ observed in the PSBL and subtract the lobe influence from it. We use the same area as the lobe entry: 10 R_E × 30 R_E for streaming O^+ coming from northern and southern hemispheres. The PSBL fluence is then the product of PSBL density, velocity perpendicular to the entry surface and the areas. The median and quartile values are shown in Table 1 and the calculated fluence can be found in Table 2. As mentioned earlier, data used in this study is collected when F10.7 is below 100 sfu.

Ion Species	F10.7	Lobe Input [10^24 /s]	Tail Input [10^24 /s]	Auroral Input [10^24 /s]	Total Input [10^24 /s]	Output [10^24 /s]
H^+ density	All	17.5 [6.96, 32.2]	29.2 [18.6, 42.0]	Unknown	46.7 [25.6, 74.2]	54.8 [29.8, 83.5]
O^+ density	< 100	0.48 [0.21, 0.90]	0.56 [0.46, 0.66]	2.59 [1.51, 5.21]	3.62 [2.18, 6.77]	4.07 [1.82, 7.07]
	> 100	1.09 [0.45, 2.99]	1.20 [0.27, 3.63]	Unknown	2.30 [0.72, 6.62]	10.5 [5.1, 17.5]

Table 2. The estimation results of the slab model, using data from Table 1. The sum of inputs is the total fluence of lobe input, tail input and auroral input. Values in the bracket show the quartiles of the value.

Table 2 shows the estimated fluence of input of the lobe, entry from the more distant magnetotail, auroral outflow, and the loss into the inner magnetosphere. Cully et al. 2003 showed that the influence of O^+ outflow correlates strongly with F10.7, which is not true for H^+. The influence of O^+ net outflow is ~10 times higher above 125 sfu than below 125 sfu. Thus, the fluence calculation of O^+ is done for F10.7 above and below 100 sfu. The total fluence of H^+ input from the lobe (1.75×10^{25} s^{-1}) and magnetotail (2.92×10^{25} s^{-1}) accounts for ~85% of the total ion fluence (5.48×10^{25} s^{-1}) into the inner magnetosphere. Although the error bar is large because the data is collected from references using long-term data, it clearly supports that ions from the lobes and the more distant magnetotail, are the dominant sources for plasma sheet H^+.

The auroral outflows may contribute but are not likely to be substantial. Nowrouzi et al. (2023) shows that the H^+ outflow is on the same order as the O^+ outflow, implying that the fluence of the auroral outflowing H^+ is on the order of 10^{24} s^{-1}, much lower than the other sources.

In contrast, for O^+, the nightside auroral source is more important. When F10.7 is low, the total fluence of O^+ from the lobe (4.8×10^{23} s^{-1}) and tail (5.6×10^{23} s^{-1}) input accounts for only ~26% of the O^+ that convects towards the inner magnetosphere. The estimated fluence of auroral source O^+ (2.59×10^{24} /s) is larger than the total of lobe and tail input even considering the errors, indicating that auroral source O^+ is a definite major source (~72%) to the quiet-time hot plasma sheet O^+. The total of all the known inputs is at 3.62×10^{24} /s, which is comparable to output at 4.07×10^{24}, considering the variance. We note that this estimate of O^+ from the auroral oval is consistent with the pre-storm nightside auroral O^+ outflow observed by the FAST spacecraft (Nowrouzi et al., 2023). Although the low energy O^+ ions may not be able to contribute to the hot plasma sheet as they lack chances to accelerate, the estimate of O^+ lower than 100 eV (2.8×10^{23} s^{-1}), not shown in the paper, is only a small fraction of the total auroral outflowing O^+.

When F10.7 is above 100, we do not have data for estimation for O^+ from the auroral region. We can then determine the importance of the nightside auroral outflow contribution by comparing the ion entry from the magnetotail and the lobes to the ion loss near the Earth. The total influence of lobe and tail inputs (2.30×10^{24} s^{-1}) makes ~22% of the output fluence (10.5×10^{24} s^{-1}) of O^+ to the inner magnetosphere, which is even lower than the same contribution (26%) for low F10.7. The result implies that, during non-storm time, O^+ from nightside auroral outflows provides a significant fraction of the plasma sheet O^+ at 7 R_E, regardless of EUV levels, and when F10.7 is higher, the auroral outflowing o^+ has an even stronger contribution.

It is important to point out again that the estimations here are based on the median values, which is dominated by the non-storm time condition. The contribution of storm time O^+ could be quite different, due to a much-enhanced dayside cusp outflow and a much more dynamics magnetosphere. Kistler et al. 2010 shows that during storm time, the density of lobe beams can reach as high as 0.1 cm^{-3}, more than 10 times of the quiet time value. Hence, it is still possible that cusp origin O^+ takes over and becomes the major contribution of the O^+ in the hot plasma sheet during storm time.

Acknowledgments

The work at the University of New Hampshire is supported by the NASA GI MMS 80NSSC17K0643, the NASA LWS 80NSSC19K0073, the NSF ANSWERS 2149787 and NSF GEM 2247712.

Open Research

Original MMS satellite data are avliable at https://lasp.colorado.edu/mms/sdc/public/. Streaming O^+ extracted and assocated processed data are available at https://zenodo.org/records/10815491 (Liao et al. 2024). The software developed to extract streaming O+ and relavant data, and create data visualization is in IDL and avalaible at https://github.com/shihikoo/mms_oplus_beam.

References

Angelopoulos, V., Kennel, C. F., Coroniti, F. V., Pellat, R., Spence, H. E., Kivelson, M. G., et al. (1993). Characteristics of ion flow in the quiet state of the inner plasma sheet. *Geophysical Research Letters*, *20*(16), 1711–1714. https://doi.org/10.1029/93GL00847

Chen, M. W., Wang, C.-P., Schulz, M., & Lyons, L. R. (2007). Solar-wind influence on MLT dependence of plasma sheet conditions and their effects on storm time ring current formation. *Geophysical Research Letters*, *34*(14), L14112. https://doi.org/10.1029/2007GL030189

Chong, G. S., Pitkänen, T., Hamrin, M., & Schillings, A. (2021). Ion Convection as a Function of Distance to the Neutral Sheet in Earth's Magnetotail. *Journal of Geophysical Research: Space Physics*, *126*(12). https://doi.org/10.1029/2021JA029694

Cladis, J. B. (1986). Parallel acceleration and transport of ions from polar ionosphere to plasma sheet. *Geophysical Research Letters*, *13*(9), 893–896. https://doi.org/10.1029/GL013i009p00893

Cully, C. M., Donovan, E. F., Yau, A. W., & Arkos, G. G. (2003). Akebono/Suprathermal Mass Spectrometer observations of low-energy ion outflow: Dependence on magnetic activity and solar wind conditions. *Journal of Geophysical Research: Space Physics*, *108*(A2), 2001JA009200. https://doi.org/10.1029/2001JA009200

Elliott, H. A., Comfort, R. H., Craven, P. D., Chandler, M. O., & Moore, T. E. (2001). Solar wind influence on the oxygen content of ion outflow in the high-altitude polar cap during solar minimum conditions. *Journal of Geophysical Research: Space Physics*, *106*(A4), 6067–6084. https://doi.org/10.1029/2000JA003022

Engwall, E., Eriksson, A. I., Cully, C. M., André, M., Torbert, R., & Vaith, H. (2009). Earth's ionospheric outflow dominated by hidden cold plasma. *Nature Geoscience*, *2*(1), 24–27. https://doi.org/10.1038/ngeo387

Gkioulidou, M., Ohtani, S., Ukhorskiy, A. Y., Mitchell, D. G., Takahashi, K., Spence, H. E., et al. (2019). Low-Energy (<keV) O^+ Ion Outflow Directly Into the Inner Magnetosphere: Van Allen Probes Observations. *Journal of Geophysical Research: Space Physics*, *124*(1), 405–419. https://doi.org/10.1029/2018JA025862

Haaland, S., Paschmann, G., Förster, M., Quinn, J., Torbert, R., Vaith, H., et al. (2008). Plasma convection in the magnetotail lobes: statistical results from Cluster EDI measurements. *Annales Geophysicae*, *26*(8), 2371–2382. https://doi.org/10.5194/angeo-26-2371-2008

Huddleston, M. M., Chappell, C. R., Delcourt, D. C., Moore, T. E., Giles, B. L., & Chandler, M. O. (2005). An examination of the process and magnitude of ionospheric plasma supply to the magnetosphere. *Journal of Geophysical Research*, *110*(A12), A12202. https://doi.org/10.1029/2004JA010401

Juusola, L., Østgaard, N., Tanskanen, E., Partamies, N., & Snekvik, K. (2011). Earthward plasma sheet flows during substorm phases: PS FLOWS DURING SUBSTORMS. *Journal of Geophysical Research: Space Physics*, *116*(A10), n/a-n/a. https://doi.org/10.1029/2011JA016852

Juusola, L., Østgaard, N., & Tanskanen, E. (2011). Statistics of plasma sheet convection: PS STATISTICS. *Journal of Geophysical Research: Space Physics*, *116*(A8), n/a-n/a. https://doi.org/10.1029/2011JA016479

Keika, K., Kistler, L. M., & Brandt, P. C. (2013). Energization of O^+ ions in the Earth's inner magnetosphere and the effects on ring current buildup: A review of previous observations and possible mechanisms: A REVIEW OF O^+ ENERGIZATION. *Journal of Geophysical Research: Space Physics*, *118*(7), 4441–4464. https://doi.org/10.1002/jgra.50371

Kistler, L. M., & Mouikis, C. G. (2016). The inner magnetosphere ion composition and local time distribution over a solar cycle: Cluster Ion Composition. *Journal of Geophysical Research: Space Physics*, *121*(3), 2009–2032. https://doi.org/10.1002/2015JA021883

Kistler, L. M., Ipavich, F. M., Hamilton, D. C., Gloeckler, G., Wilken, B., Kremser, G., & Stüdemann, W. (1989). Energy spectra of the major ion species in the ring current during geomagnetic storms. *Journal of Geophysical Research: Space Physics*, *94*(A4), 3579–3599. https://doi.org/10.1029/JA094iA04p03579

Kistler, L. M., Mouikis, C. G., Cao, X., Frey, H., Klecker, B., Dandouras, I., et al. (2006). Ion composition and pressure changes in storm time and nonstorm substorms in the vicinity of the near-Earth neutral line. *Journal of Geophysical Research*, *111*(A11), A11222. https://doi.org/10.1029/2006JA011939

Kistler, L. M., Mouikis, C. G., Klecker, B., & Dandouras, I. (2010). Cusp as a source for oxygen in the plasma sheet during geomagnetic storms: OXYGEN IN THE PLASMA SHEET-CUSP SOURCE. *Journal of Geophysical Research: Space Physics*, *115*(A3), n/a-n/a. https://doi.org/10.1029/2009JA014838

Kistler, L. M., Mouikis, C. G., Asamura, K., Yokota, S., Kasahara, S., Miyoshi, Y., et al. (2019). Cusp and Nightside Auroral Sources of O^+ in the Plasma Sheet. *Journal of Geophysical Research: Space Physics*, *124*(12), 10036–10047. https://doi.org/10.1029/2019JA027061

Liao, J., Kistler, L. M., Mouikis, C. G., Klecker, B., Dandouras, I., & Zhang, J.-C. (2010). Statistical study of O^+ transport from the cusp to the lobes with Cluster CODIF data: O^+ TRANSPORT STATISTICAL STUDY. *Journal of Geophysical Research: Space Physics*, *115*(A12), n/a-n/a. https://doi.org/10.1029/2010JA015613

Liao, Jing. (2011). Statistical study of oxygen transport from the cusp to the plasmasheet. *Doctoral Dissertations*. Retrieved from https://scholars.unh.edu/dissertation/642

Liao, J., Kistler, L., & Mouikis, C. (2024). Streaming O+ data from MMS/HPCA [Data set]. *Zenodo*. https://doi.org/10.5281/zenodo.10815491

Liu, Z. -Y., & Zong, Q. -G. (2022). Ionospheric Oxygen Outflows Directly Injected Into the Inner Magnetosphere: Van Allen Probes Statistics. *Journal of Geophysical Research: Space Physics*, *127*(10). https://doi.org/10.1029/2022JA030611

Maggiolo, R., & Kistler, L. M. (2014). Spatial variation in the plasma sheet composition: Dependence on geomagnetic and solar activity: O^+ and H^+ density in the plasmasheet. *Journal of Geophysical Research: Space Physics*, *119*(4), 2836–2857. https://doi.org/10.1002/2013JA019517

Miyashita, Y., Seki, K., Sakaguchi, K., Hiraki, Y., Nosé, M., Machida, S., et al. (2020). On the Transition Between the Inner and Outer Plasma Sheet in the Earth's Magnetotail. *Journal of Geophysical Research: Space Physics*, *125*(4). https://doi.org/10.1029/2019JA027561

Moore, T. E., Chandler, M. O., Chappell, C. R., Comfort, R. H., Craven, P. D., Delcourt, D. C., et al. (1999). Polar/TIDE results on polar ion outflows. In L. Burch, L. Carovillano, & K. Antiochos

(Eds.), *Geophysical Monograph Series* (Vol. 109, pp. 87–101). Washington, D. C.: American Geophysical Union. https://doi.org/10.1029/GM109p0087

Moore, T. E., Fok, M.-C., Christon, S. P., Chen, S.-H., Chandler, M. O., Delcourt, D. C., et al. (2005). Solar and ionospheric plasmas in the ring current region. In J. Burch, M. Schulz, & H. Spence (Eds.), *Geophysical Monograph Series* (Vol. 159, pp. 179–194). Washington, D. C.: American Geophysical Union. https://doi.org/10.1029/159GM14

Mouikis, C. G., Kistler, L. M., Liu, Y. H., Klecker, B., Korth, A., & Dandouras, I. (2010). H^+ and O^+ content of the plasma sheet at 15-19 Re as a function of geomagnetic and solar activity: THE PLASMA SHEET H^+ AND O^+ CONTENT. *Journal of Geophysical Research: Space Physics*, *115*(A12), n/a-n/a. https://doi.org/10.1029/2010JA015978

Nosé, M., McEntire, R. W., & Christon, S. P. (2003). Change of the plasma sheet ion composition during magnetic storm development observed by the Geotail spacecraft. *Journal of Geophysical Research: Space Physics*, *108*(A5), 2002JA009660. https://doi.org/10.1029/2002JA009660

Nowrouzi, N., Kistler, L. M., Zhao, K., Lund, E. J., Mouikis, C., Payne, G., & Klecker, B. (2023). The Variation of Ionospheric O^+ and H^+ Outflow on Storm Timescales. *Journal of Geophysical Research: Space Physics*, *128*(11), e2023JA031786. https://doi.org/10.1029/2023JA031786

Sauvaud, J.-A. (2004). Case studies of the dynamics of ionospheric ions in the Earth's magnetotail. *Journal of Geophysical Research*, *109*(A1), A01212. https://doi.org/10.1029/2003JA009996

Seki, K., Elphic, R. C., Thomsen, M. F., Bonnell, J., Lund, E. J., Hirahara, M., et al. (2000). Cold flowing O^+ beams in the lobe/mantle at Geotail: Does FAST observe the source? *Journal of Geophysical Research: Space Physics*, *105*(A7), 15931–15944. https://doi.org/10.1029/1999JA900470

Strangeway, R. J., Ergun, R. E., Su, Y.-J., Carlson, C. W., & Elphic, R. C. (2005). Factors controlling ionospheric outflows as observed at intermediate altitudes. *Journal of Geophysical Research: Space Physics*, *110*(A3). https://doi.org/10.1029/2004JA010829

Torbert, R. B., Russell, C. T., Magnes, W., Ergun, R. E., Lindqvist, P.-A., LeContel, O., et al. (2016). The FIELDS Instrument Suite on MMS: Scientific Objectives, Measurements, and Data

Products. *Space Science Reviews*, *199*(1–4), 105–135. https://doi.org/10.1007/s11214-014-0109-8

Young, D. T., Burch, J. L., Gomez, R. G., De Los Santos, A., Miller, G. P., Wilson, P., et al. (2016). Hot Plasma Composition Analyzer for the Magnetospheric Multiscale Mission. *Space Science Reviews*, *199*(1–4), 407–470. https://doi.org/10.1007/s11214-014-0119-6

Zhao, K., Kistler, L. . m., Lund, E. J., Nowrouzi, N., Kitamura, N., & Strangeway, R. J. (2020). Factors Controlling O^+ and H^+ Outflow in the Cusp During a Geomagnetic Storm: FAST/TEAMS Observations. *Geophysical Research Letters*, *47*(11), e2020GL086975. https://doi.org/10.1029/2020GL086975

Zhao, K., Kistler, L. M., Lund, E. J., Nowrouzi, N., Kitamura, N., & Strangeway, R. J. (2022). Nightside Auroral H^+ and O^+ Outflows Versus Energy Inputs During a Geomagnetic Storm. *Journal of Geophysical Research: Space Physics*, *127*(11). https://doi.org/10.1029/2022JA030923

Appendix

Appendix A: Impact of Compression Scheme

The compression scheme of HPCA drops the least significant bit in any accumulated energy-angle-angle bin for each species before downlinked to the ground, which eliminates data from any bins with single counts. This can result in significantly lower flux. Under Survey mode, the bit is dropped after summation; under Burst mode, since there is no summation, so there are more bins with single counts, hence the impact is greater for Burst mode than Survey mode. The impact is greater for isotropic populations than for anisotropic populations for the same total number of counts. The flux reduction is most significant for minor species and low energy populations as they have lower counts. The compression was temporarily off under Fast Survey mode [Young et al., 2016] from 2018-05-27 to 2018-09-25 and for the entire orbit from 2019-04-16 to 2019-08-17. The lossy scheme was turned off after 2022-05-24.

To analyze the impact of the compression scheme and to restore the occurrence frequency to the original level, we simulated the compression algorithm and apply it to the data from a period when the compression scheme was off during 2018 and 2019: Fast Survey mode from 2018-05-27 to 2018-09-25, for the entire orbit from 2019-04-16 to 2019-08-17.

By comparing the occurrence frequency maps with and without the compression for the same period, we calculated empirical occurrence frequency correction factors depending on the observed occurrence frequency. Figure A1 shows how the correction factor depends on the occurrence frequency for the lobes, PSBL, and the plasma sheet. As expected, the correction factors are above one, which means the occurrence frequency with the compressed data is much lower than the actual value, and the loss is more significant for lower occurrence frequency. To compensate for the loss, for all the occurrence frequency maps presented in this paper, we apply the piecewise-linear factors shown by the black lines in Figure A1 as a correction to bring the occurrence frequency closer to the true value. The correction factors here are applied to all the occurrence frequency maps in the paper except Figure 7, which applies the energy-depending correction factors in Figure A3.

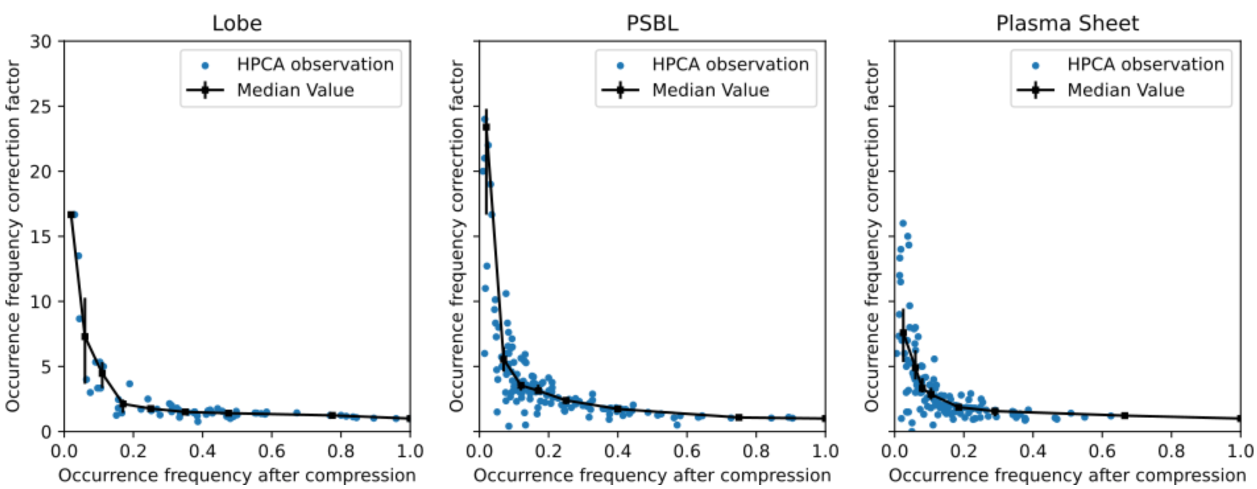

Figure A1. Dependence of the Occurrence frequency compression correction factor on the occurrence frequency observed after compression, for different regions.

Figure A2 shows the original, after compression and after correction occurrence frequency maps, with the data collected during non-compression time during 2018-2019. The occurrence frequency of the streaming O^+ is clearly reduced after the compression. After applying the correction factors, the overall occurrence frequency goes back to the original level and the pattern of the occurrence frequency map remains.

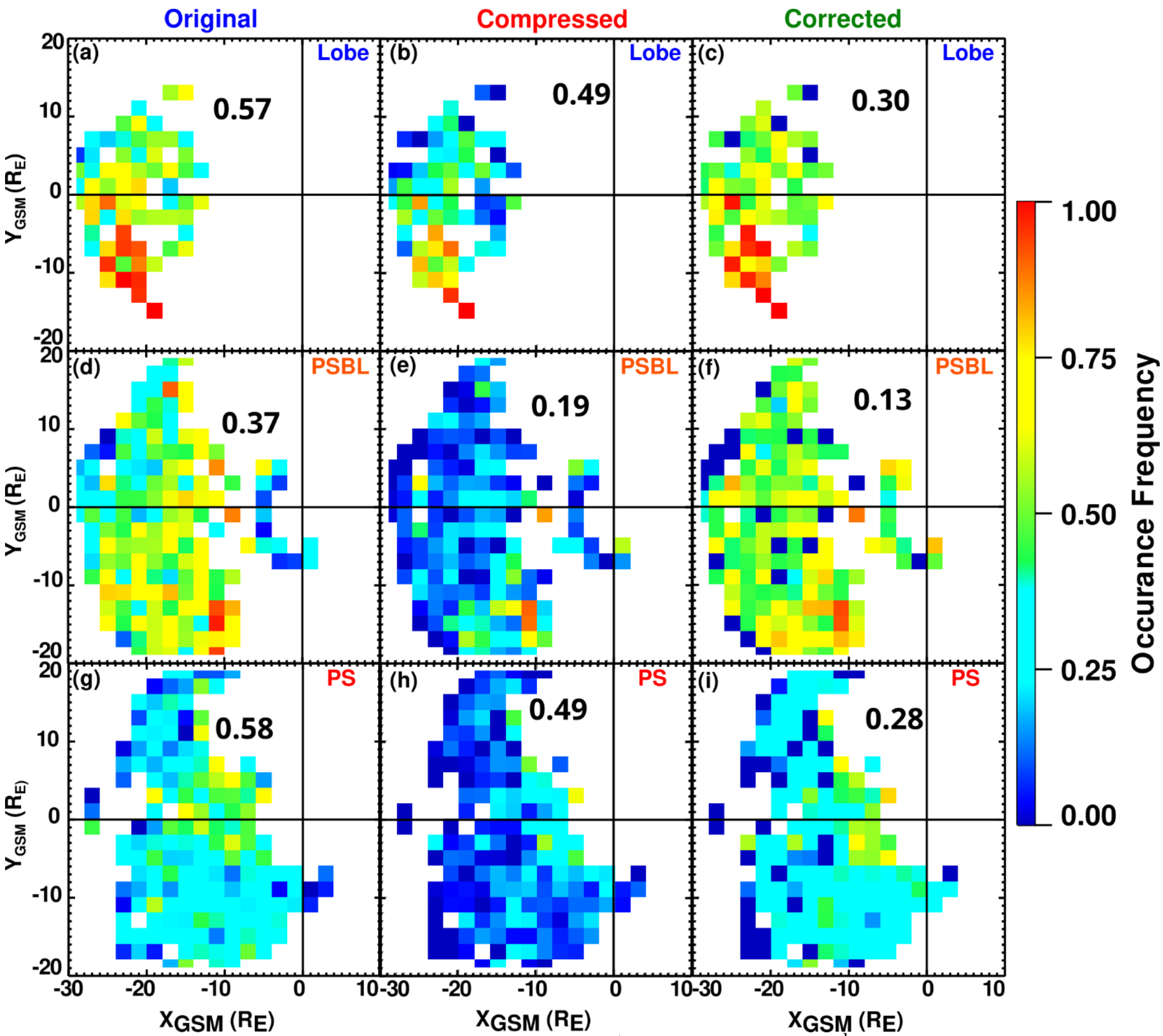

Figure A2. Occurrence frequency maps without (1st column), with (2nd column) simulated compression, and with correction factors applied on compressed data (3rd column). Rowsfrom left to right are in lobes, the PSBL, and the PS. Data collected during the non-compression time during 2018-2019.

Considering the energy dependence of the compression scheme impact, we also calculated the correction factors with energy dependence, as shown in Figure A3. This group of factors are applied to the occurrence frequency maps in Figure 7.

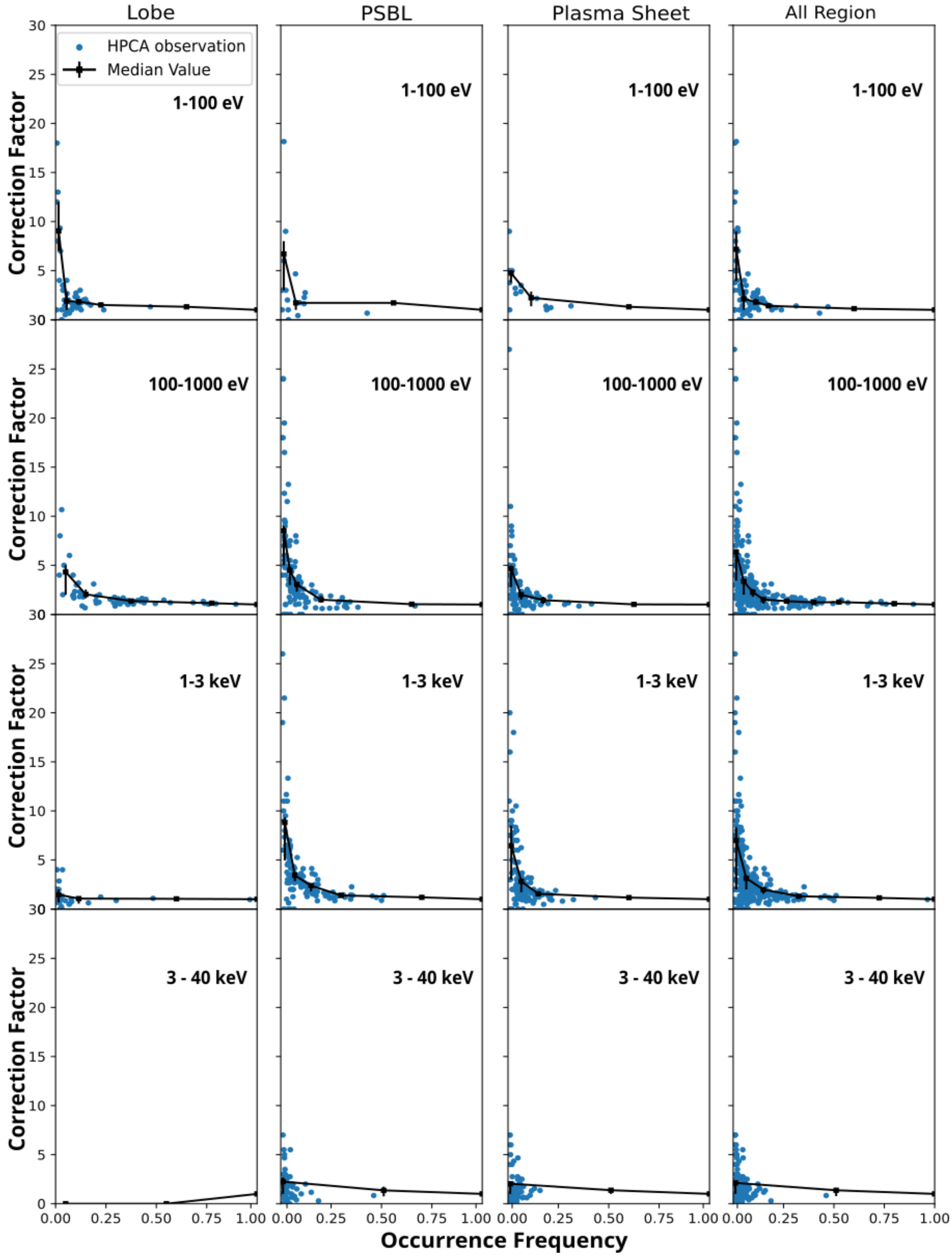

Figure A3. Dependence of the Occurrence frequency compression correction factor on the occurrence frequency observed after compression, sorted by energy range (rows) 1 - 100 eV, 100

- 1000 eV, 1-3 keV and > 3 keV, and by different regions (columns). Blue dots are the observations, and the black lines show the median value and quartile of the data.

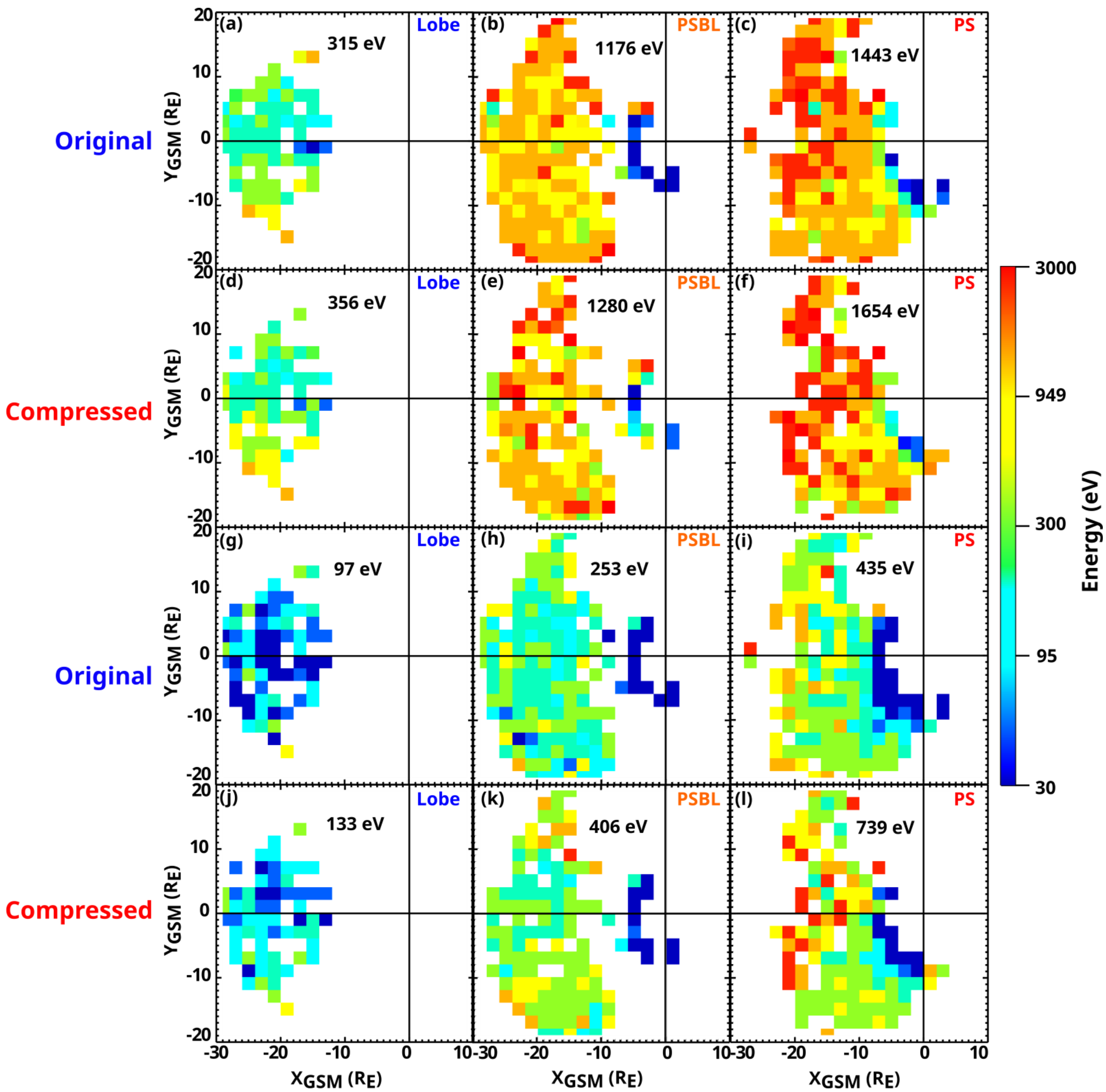

Figure A4. Median energy maps without (1st row) and with (2nd row) simulated compression, and minimum energy maps without (3rd row) and with (4th row) simulated compression. Columns from left to right are in lobes, the PSBL, and the PS. The numbers are the averaged value of the energy in each map. Data collected during the non-compression time during 2018-2019.

We also studied the compression scheme's impact on the median and minimum energy maps. Figure A4 shows the comparisons of median energy and minimum energy maps with and without simulated compression scheme, with data collected during the non-compression time during 2018-2019. Maps are split into different regions as different columns: lobe, PSBL, and PS. The numbers are the averaged value of the energy in each map. The median energy maps present the averaged value of the energies of all streaming O^+ identified in one grid. Comparison of median energy maps of streaming O^+ using data without compression (1st row of Figure A4) and with simulated compression (2nd row of Figure A4) shows that, in all regions, the median value of the energy is higher when the data is compressed. The increase is smallest for lobes and higher for PSBL and the highest in the plasma sheet. However, the general patterns remain for the median energy maps for all regions. The minimum energy maps show the minimum value of the energy of all streaming O^+ observed in one bin. There is a clear increase in the minimum energy when data is compressed (4th row of Figure A4). The increase is smaller in the lobes (Figure A4j) and larger in the more isotropic regions (Figure A4k-l). In the PSBL and PS maps, the population near the Earth with energy around or lower than 30 eV remained in Figure A4k and A4i. The energy spatial profile is similar with and without compression. The count rate in the instrument is proportional to the energy flux, so the count rate is much lower for the low energy data than energetic data. As a result, the compression scheme that drops all the single-count data has a greater impact on the low-energy channels. When low-energy streaming O^+ ions are missing, the aggregated median energy is higher, and the observed minimum energy is much higher. Because the streaming population is anisotropic inside the lobes and gets scattered as it enters the denser part of the magnetosphere, the lobe streaming O^+ is less impacted by the compression scheme than the streaming O^+ in the PSBL and the PS. Due to the high density of the near-Earth nightside streaming O^+, their profile remains in the energy maps.

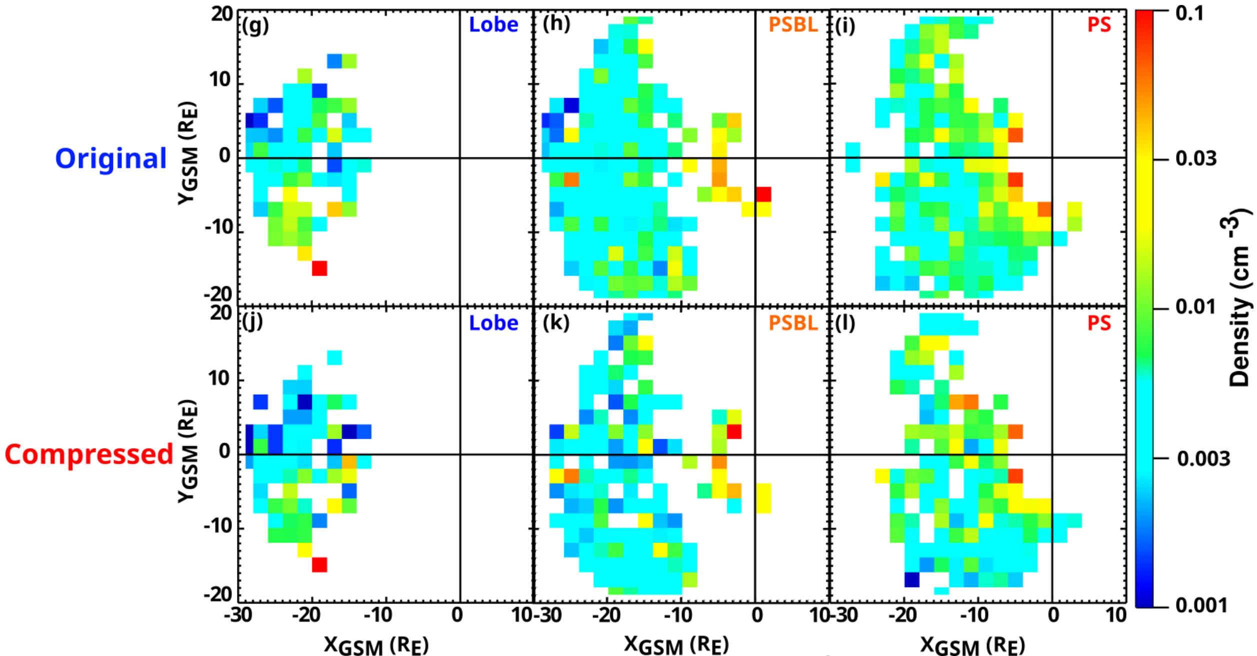

Figure A5. Median density maps without (1st row) and with (2nd row) simulated compression. Columns from left to right are in lobes, the PSBL, and the PS. The numbers are the averaged value of the energy in each map. Data collected during the non-compression time during 2018-2019.

Figure A5 shows the comparison between the original density maps and those after compression, with same data as earlier comparisons. The compression scheme does not have a strong impact on the density maps. Both the median values and the patterns remain with the compression scheme on. While the density effect is not large for the anisotropic beam populations analyzed in this study, the average effect on O^+ in the isotropic plasma sheet population is a factor of 10, and can be as high as a factor of 100.